ORTHOGONAL AND SYMMETRIC HAAR WAVELETS ON THE THREE-DIMENSIONAL BALL

by

Andy Chow

A thesis submitted in conformity with the requirements
for the degree of Master of Science
Graduate Department of Computer Science
University of Toronto

Abstract

ORTHOGONAL AND SYMMETRIC HAAR WAVELETS ON THE THREE-DIMENSIONAL BALL

Andy Chow

Master of Science

Graduate Department of Computer Science

University of Toronto

2010

Spherical signals can be found in a wide range of fields, including astronomy, computer graphics, medical imaging and geoscience. An efficient and accurate representation of spherical signals is therefore essential for many applications. For this reason, we derive a novel wavelet basis called *3D SOHO*. It is the first Haar wavelet basis on the three-dimensional spherical solid that is both orthogonal and symmetric. These theoretical properties allow for a fast wavelet transform, optimal approximation, perfect reconstruction and other practical benefits. Experimental results demonstrate the representation performance of 3D SOHO on a variety of volumetric spherical signals, such as those obtained from medical CT, brain MRI and atmospheric model. The approximation performance of 3D SOHO is also empirically compared, against that of Solid Harmonic, 3D Haar wavelet transform and 3D discrete cosine transform.

Acknowledgements

I would like to thank my friends and family for their love and support, especially my parents, Mark and Agnes.

I would also like to thank my mentors and colleagues for their guidance in my academic endeavors. I am grateful to Virginijus Barzda, Eugene Fiume, John Hancock, Aaron Hertzmann, Allan Jepson, Christian Lessig, Derek Nowrouzezahrai, Arnold Rosenbloom, Sami Siddique and Ian Vollick.

Many thanks to Dr. David Jaffray and the Image Guided Therapy lab at Princess Margaret Hospital for providing the CT data.

Finally, I would like to thank the Ontario Graduate Scholarship (OGS) program and the Graduate Department of Computer Science at the University of Toronto for their generous financial support.

Contents

Chapter 1

Introduction

Wavelets have been successfully used in many areas of science, mathematics and engineering. Examples include astronomy [7, 25, 27, 62, 79, 80], bioinformatics [6, 10, 40, 44, 63], computer graphics [5, 15, 43, 50, 72, 81] and geoscience [35, 56, 77, 87]. The list of applications continues to grow, as researchers develop new wavelets with different capabilities and attributes. In this thesis, we introduce a novel wavelet for representing signals over the unit ball. Potential applications can be found in seismology [2, 11, 29, 58], medical imaging [64, 65, 97, 99], astrophysics [42, 53, 54, 92, 91] and other fields where signals are naturally parameterized in spherical coordinates.

The remainder of this chapter is devoted to a brief introduction to wavelets. We begin by explaining the basic idea behind signal representations. Following that, we identify the characteristics of wavelets that are valuable for our purposes. The chapter concludes with an overview of related work on the representation of volumetric spherical signals.

1.1 Signal Representation

Put simply, a *signal* is a mathematical function. In the physical world, any quantity that depends on time or space can be considered as a signal. For instance, a seismometer measures a signal by relating ground displacement over time. An x-ray image is another concrete example, where radiation intensity is mapped to spatial positions.

A signal can be represented in a variety of ways, often in the form of a graph, a formula or an algorithm. In the following chapters, we will propose a set of basis functions to represent functions on the three-dimensional ball. This method of representation is analogous to the way that a vector can be written as a linear combination of basis vectors.

Any function in the space spanned by the basis functions can be represented as a unique sequence of basis function coefficients. The process of transforming a signal to a basis representation is called *projection*, while the reverse process of synthesizing a signal from the basis function coefficients is called *reconstruction*. Intuitively, a basis function coefficient determines the amount of contribution made by a basis function to the basis representation. Equivalently, a basis function coefficient measures the similarity between a basis function and the signal. The properties and limitations of a basis are hence determined by its span and the characteristics of its basis functions. In the following section we will identify basis properties that are desirable for our purposes.

1.2 Wavelets

The historical development of wavelets has been well-documented in the literature [19, 38, 41, 55], and many comprehensive introductions have been written on the subject [16, 20, 31, 86, 93]. Nevertheless, a universally accepted definition for *wavelet* has never been established, perhaps due to its diversity and continual evolution. Rather than to offer a precise definition, we will describe wavelets in terms of the main features that they have in common. In Wim Sweldens' seminal work on the lifting scheme, he characterizes wavelets as [84]:

> "... building blocks that can quickly decorrelate data.".

Sweldens' description incorporates three main features of wavelets. First, wavelets are analogous to *building blocks*. They form a basis in which signals can be represented as a linear combination of wavelet basis functions. The basis functions of wavelets also have very similar structure and therefore resemble *blocks*. In fact, the basis functions of a first generation wavelet are dilates and translates of a mother wavelet function.

Next, the word "quickly" refers to the existence of fast algorithms for signal analysis and synthesis. These algorithms can transform a signal between its original representation and its wavelet representation in time that depends linearly on the size of the signal. This speed efficiency is accomplished by regarding the wavelets as filter banks. Then the basis function coefficients can be obtained using filters, rather than expensive inner products between the dual basis functions and the signal.

Finally, wavelets can decorrelate data so that the wavelet representation is more "compact" than the original representation. Most of the wavelet basis function coefficients

are small in magnitude because most of the energy is concentrated in a few coefficients. Unlike random noise, natural signals are correlated in space and frequency. For instance, two adjacent pixels in an image are typically similar relative to those that are spaced far apart. Similarly, frequencies often occur in bands. Natural signals tend to exhibit a correlation structure that is localized in space, and decay toward both ends of the frequency spectrum. We can exploit this structure to obtain compact representations, where a large percentage of the wavelet coefficients are close to zero in magnitude. The idea of wavelets is to design basis functions that capture local differences in a signal. Then a large wavelet coefficient indicates a large degree of dissimilarity between the signal and the wavelet basis function. Compact representations are desirable because we can obtain accurate approximations by ignoring the small coefficients. In effect, prominent features are maintained in the approximation while insignificant details are discarded.

1.3 Related Work

Over the years, different bases and frames have been developed to represent, approximate, analyze and process signals parameterized in spherical coordinates. However, the vast majority of those techniques are designed for signals on the sphere $\mathbb{S}^2$. In contrast, there are relatively few bases for signals on the three-dimensional ball $\mathbb{B}^3$.

Most of the representations for square-integrable functions in $L_2(\mathbb{B}^3)$ can be classified into three families, based on ridgelets, spherical harmonics and splines, respectively. In the following, we will provide an overview of each family, and then introduce the direct predecessor of our technique.

1.3.1 Ridgelets

Ridge functions appear naturally in various areas including tomography, statistics and neural networks. They are multivariate functions $f : \mathbb{R}^2 \to \mathbb{R}$ of the form $f(x, y) = r(ax + by)$, where $(a, b) \in \mathbb{R}^2$ is called the *direction* [37, 39]. Geometrically, the level sets of ridge function f are lines $t = ax+by$, and thus the graph of f exhibits ridges [24]. The function $g(t)$ is the profile of f in the plane orthogonal to lines t. A *ridgelet* is a ridge function whose profile is a wavelet.

In essence, a ridgelet is a regular two-dimensional wavelet that is constant along a preferred direction [3]. Ridgelets exhibit high directional sensitivity due to their anisotropic nature. Therefore, ridgelet transform provides efficient representations for signals that are smooth away from line singularities. In contrast, wavelet bases are only efficient in representing signals that are smooth away from point singularities. As an illustration, consider the representation of an edge in an image. A ridgelet can simply align its preferred direction with the principal direction of the edge, whereas many wavelets may be needed to "pave" along the edge. For this reason, ridgelet analysis has been employed to deal with higher-dimensional discontinuities, such as those found in astrophysics [79, 80, 78] and medical imaging [21, 76, 75].

Candès [8] developed the first ridgelet transform for functions $f \in L_2(D)$, where D is a compact set in $\mathbb{R}^d$. The ridgelet transform corresponds to wavelet analysis in the Radon domain [9]. It allows for stable representations and approximations of f, as a superposition of ridgelets that form a frame for $L_2(D)$, which can be regarded as an overcomplete basis. Donoho extended the idea of ridgelets to obtain the first orthonormal ridgelet basis for $L_2(\mathbb{R}^2)$ [23]. The pioneering work of Candès eventually lead to the development of a tight frame for $L_2(\mathbb{B}^d)$ based on ridgelets [70].

Every signal has a unique representation in an orthogonal basis, given by a unique sequence of basis function coefficients. In contrast, the ridgelet frame developed by Petrushev [70] is overcomplete, and thus a signal may have redundant representations. Overcompleteness has some advantageous in signal processing applications, such as robustness to noise [88]. However, fast ridgelet transform requires $O(n \log n)$ time complexity, as opposed to $O(n)$ needed for fast wavelet transform [26]. The resulting representations are also typically less compact compared to those in an orthogonal basis.

1.3.2 Spherical Harmonics

Spherical harmonics are the angular portion of an orthogonal set of solutions to Laplace's equation on the sphere [74]. They can be regarded as spherical analogs of the Fourier basis. Several complete orthonormal systems in $L_2(\mathbb{B}^3)$ have been formulated based on spherical harmonics. These systems employ spherical harmonics in angular dimension, in combination with orthogonal polynomials in radial dimension.

Spherical harmonic bases for $L_2(\mathbb{B}^3)$ have been used to model seismic wave velocity in the Earth's mantle [51, 83]. The lateral parameterization is provided by spherical harmonics, while the radial component is modeled by Chebyshev polynomials or cubic B-splines. Orthogonal bases formed by spherical harmonics and Jacobi polynomials have also been used to derive reproducing kernels [90] and wavelets on the three-dimensional ball [59]. Such wavelets have been applied in the recovery of the Earth's harmonic density distribution from gravitational data [57, 58].

The spherical harmonic basis functions have global support, which prevents their localization in space. Consequently, spherical harmonics are not suitable for the repre-

sentation of high frequency signals. An order n approximation in spherical harmonics require n^2 coefficients, and a fast transform for spherical harmonics has computational complexity of $O(n \log n)$ [61]. The results often exhibit ringing artifacts [32, 66, 94].

1.3.3 Splines

Spline bases have been used extensively in geoscience to represent and analyze signals on $\mathbb{B}^3$. They have been employed to solve the inverse gravimetry problem of determining the Earth's density distribution from gravitational data obtained by satellites. The inverse gravimetry problem is exponentially ill-posed, and harmonic spline-wavelets provide a regularization method for yielding stable approximations of harmonic density functions on $\mathbb{B}^3$ [29, 58, 60]. Multiresolution representations are generated by reducing the hat-width of spline wavelet basis functions rather than by scaling functions.

In addition to the inverse gravimetry problem, splines have also been used to model seismic waves on $\mathbb{B}^3$. The travel-time of earthquake waves are measured at various seismic stations around the globe, and seismic tomography analyzes the travel-times to determine the velocity field inside the Earth. The velocity field helps to infer the interior structure of the Earth, since wave propagation speed depends on temperature, density, mineral structure and composition [33]. Two different spline techniques are used to approximate the velocity field inside the Earth. The first approach uses harmonic spherical splines, based on a reproducing kernel Hilbert space mentioned in the previous section [1]. The second approach uses spherical B-splines for lateral parameterization, and cubic B-splines for radial parameterization [4, 34].

Spline basis functions with local support can avoid some of the performance issues with spherical harmonics. There are spline basis transforms with linear computational complexity, and the resulting representations are more compact than those of spherical harmonics [36]. However, the smooth nature of spline basis functions makes it less efficient at representing high-frequency signals.

1.3.4 Wavelets

Our objective is to develop a basis for efficiently representing all-frequency signals on $\mathbb{B}^3$. In particular, we want fast transform algorithms and compact representations. Techniques based on ridgelets, spherical harmonics or splines are unsuitable due to the drawbacks discussed in the previous sections. Instead, we will extend an existing discrete wavelet basis called *SOHO* (cf. [48]) which is known to be a suitable basis for representing all-frequency signals defined over the sphere $\mathbb{S}^2$ [47]. SOHO has many desirable theoretical properties, such as orthonormality and symmetry, which will be discussed in Chapter 3. Moreover, there are linear-time transform algorithms for SOHO, and an approximation strategy that is optimal in the ℓ_2 norm. In a later chapter, we will demonstrate a method to generalize SOHO into a basis for $L_2(\mathbb{B}^3)$ while maintaining its useful properties.

1.4 Organization

The remainder of the thesis is organized as follows. Chapter 2 provides the mathematical background, such as definitions and theorems that are used throughout the thesis. In Chapter 3, we present the SOHO wavelet basis for $L_2(\mathbb{S}^2)$. These concepts

are generalized in Chapter 4, to yield a new wavelet basis for $L_2(\mathbb{B}^3)$. The performance of 3D SOHO has been experimentally evaluated, and the methodology, results and interpretations are presented in Chapter 5. Finally, we discuss possibilities for future work in Chapter 6, and conclude the thesis in Chapter 7.

Chapter 2

Background

In this chapter we will establish the terminology and the notation for the remainder of the thesis. The reader can quickly browse through this chapter on the first reading, and refer back to this chapter when necessary.

2.1 Geometric Figures

2.1.1 Spherical Shells

A *spherical shell* is the volume between two concentric spheres of differing radii. Let shell S be the volume enclosed by concentric spheres S_1 and S_2, with radii r_1 and r_2 respectively, such that $r_1 < r_2$. Then the *thickness* t of S is defined as $t = r_2 - r_1$, and the *radius* r of S is $r = r_1 + \frac{t}{2}$. The sphere S_1 is called the *minimal bounding sphere* of S, while S_2 is the *maximal bounding sphere* of S.

Let shell S be the volume enclosed by concentric spheres S_1 and S_2, with radii r_1 and r_2 respectively, such that $r_1 < r_2$. Let S_3 be the sphere that divides shell S into two

shells with equal volumes. Then the radius r_3 of sphere S_3 is

$$r_3 = \sqrt[3]{\frac{r_1^3 + r_2^3}{2}}. \tag{2.1}$$

Equation 2.1 can be derived as follows. Let S_a and S_b be the shells obtained by dividing S into two shells with equal volumes. Without loss of generality, suppose the minimal and maximal bounding spheres of S_a has a radius of r_1 and r_3 respectively. Then the minimal and maximal bounding spheres of S_b has a radius of r_3 and r_2 respectively, and we have

$$\begin{aligned} \frac{4}{3}\pi(r_3^3 - r_1^3) &= \frac{4}{3}\pi(r_2^3 - r_3^3) \\ \Rightarrow r_3 &= \sqrt[3]{\frac{r_1^3 + r_2^3}{2}}. \end{aligned}$$

2.1.2 Spherical Triangles

A *great circle* is the intersection of a sphere with a plane that passes through the center of the sphere. Consequently, an arc of a great circle is called a *great arc*. A *spherical triangle* is formed on the surface of a sphere, by three great arcs intersecting pairwise at three vertices (Figure 2.1). The angle at a vertex is measured as the angle between the planes containing the incident great arcs.

Theorem 2.1. The area α of a spherical triangle ABC on a sphere of radius r is

$$\alpha = r^2(\angle A + \angle B + \angle C - \pi) = r^2 E, \tag{2.2}$$

where E is called the *spherical excess* of spherical triangle ABC.

Proof. See [28]. □

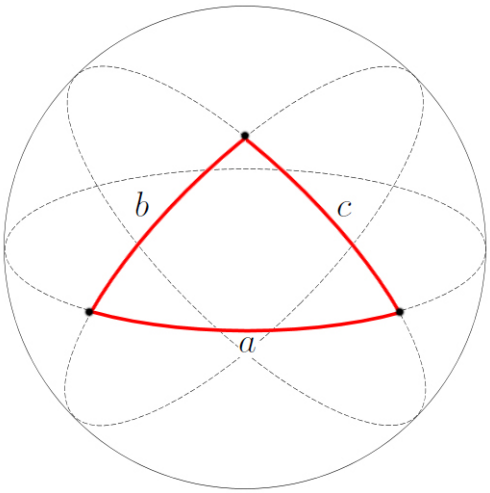

Figure 2.1: A spherical triangle formed by the great arcs a, b and c.

It is a well-known fact that the internal angles of a planar triangle always sum up to π radians. The same is not true for non-Euclidean geometries. Intuitively, the spherical excess represents the angular difference between a spherical triangle and a planar triangle with the same vertices. Notice that the spherical excess E is independent of the radius r in Equation 2.2, since the internal angles of ABC are determined by the planes of its great arcs. For example, consider the internal angle $\angle A$ between arcs b and c in Figure 2.1. It is equal to the angle between the planes that contain arcs b and c. Therefore, $\angle A$ is independent of the radius of the sphere.

2.1.3 Spherical Frusta

A *spherical frustum* is the region between two spherical triangles on a shell. More precisely, suppose F is a spherical frustum formed by spherical triangles $A_1B_1C_1$ and $A_2B_2C_2$ on the minimal and maximal bounding spheres of shell S respectively. Let

$\{A_1, A_2, O\}$, $\{B_1, B_2, O\}$, $\{C_1, C_2, O\}$ be sets of collinear points, where O is the center of S. Then $A_1B_1C_1$ and $A_2B_2C_2$ have the same spherical excess, and are located in the same hemisphere of S. Furthermore, F is the volume enclosed by edges (A_1, A_2), (B_1, B_2), (C_1, C_2), and spherical triangles $A_1B_1C_1$ and $A_2B_2C_2$.

Theorem 2.2. Let F be a spherical frustum formed by spherical triangles $A_1B_1C_1$ and $A_2B_2C_2$, on the minimal and maximal bounding spheres S_1 and S_2 of shell S respectively. Then the volume α of F is

$$\alpha = \frac{1}{3}(r_2^3 - r_1^3)E, \tag{2.3}$$

where r_1 is the radius of S_1, r_2 is the radius of S_2 and E is the spherical excess of $A_1B_1C_1$ and $A_2B_2C_2$.

Proof. The volume α of F can be found by integrating Equation 2.2 from r_1 to r_2 since the spherical excess E is independent of the radius:

$$\begin{aligned}\alpha &= \int_{r_1}^{r_2} r^2 E \mathrm{d}r \\ &= \frac{1}{3}(r_2^3 - r_1^3)E.\end{aligned}$$

□

2.1.4 Spherical Tetrahedra

A *spherical tetrahedron* is a pyramid with a spherical triangle base. Moreover, suppose S is a spherical tetrahedron defined by spherical triangle ABC on the surface of a ball centered at O. Then S is the volume enclosed by edges (A, O), (B, O), (C, O) and spherical triangle ABC. We will often use the term *spherical tetrahedron* when referring to a set of disjoint spherical frusta whose union form a spherical tetrahedron.

2.2 Abstract Algebra

2.2.1 Hilbert Spaces

Definition 2.1. A *Banach space* X is a complete normed vector space. In other words, a Banach space is a vector space over the field $\mathfrak{F}$ of real or complex numbers, with a norm $\|\cdot\|$ such that every Cauchy sequence (with respect to the metric $d(x, y) = \|x - y\|$) in X has a limit in X.

Definition 2.2. Let X be a Banach space over the field $\mathfrak{F}$ of real or complex numbers. Then the *dual space* $\tilde{X}$ of X is the Banach space of continuous linear maps $X \to \mathfrak{F}$.

Dual entities will be denoted with a tilde accent in the remainder of the thesis.

Definition 2.3. A *Hilbert space* H over field $\mathfrak{F}$ is a Banach space with an inner product $\langle \cdot, \cdot \rangle : H \times H \to \mathfrak{F}$. The inner product induces the norm $\| \cdot \| = \langle \cdot, \cdot \rangle^{1/2}$.

2.2.2 Lebesgue Spaces

Definition 2.4. Let Σ be a σ-algebra over the set X. Then a *measure* $\mu : \Sigma \to [-\infty, \infty]$ is a function that satisfies the following properties:

1. $\mu(e) \geq 0$ for all $e \in \Sigma$;
2. $\mu(\emptyset) = 0$;

3. If $\{e_i\}_{i\in I}$ is a countable collection of pairwise disjoint sets in Σ, then

$$\mu\left(\bigcup_{i\in I} e_i\right) = \sum_{i\in I} \mu\left(e_i\right).$$

The triple (X, Σ, μ) is called a *measure space*.

Definition 2.5. [49] The *Lebesgue space* L_p defined over the measure space (X, Σ, μ) is the Banach space of equivalence classes of measurable functions $f : X \to \mathbb{R}$ on (X, Σ, μ) for which the L_p-norm

$$\|f\|_p = \left(\int_X |\, f \,|^p \, \mathrm{d}\mu\right)^{1/p} < \infty,$$

where $1 \leq p < \infty$.

Definition 2.6. [71] The *Lebesgue sequence space* ℓ_p is the space of all infinite sequences $\{f_i\}_{i=1}^{\infty}$ such that the ℓ_p-norm

$$\|f\|_p = \left(\sum_{i=1}^{\infty} |\, f_i \,|^p\right)^{1/p} < \infty,$$

where $1 \leq p < \infty$.

In this thesis we will mainly focus on the space L_2 of functions with finite energy. Therefore, the notation $\|\cdot\|$ refers to the L_2-norm unless stated otherwise.

2.2.3 Bases

Definition 2.7. The *Kronecker delta* δ_{ij} is defined as

$$\delta_{i,i'} = \begin{cases} 1 & \text{if } i = i' \\ 0 & \text{otherwise.} \end{cases}$$

Definition 2.8. The elements of a sequence $\{f_i\}_{i=1}^m$ in a Hilbert space are *orthogonal* if and only if

$$\langle f_i, f_{i'} \rangle = \delta_{i,i'}, \quad \forall i, i'.$$

Definition 2.9. Two sequences $\{f_i\}_{i=1}^m$ and $\{\tilde{f}_i\}_{i=1}^m$ in a Hilbert space are *biorthogonal* if

$$\langle f_i, \tilde{f}_{i'} \rangle = \delta_{i,i'}, \quad \forall i, i'.$$

Definition 2.10. The sequence $\{e_i\}_{i=1}^m$ is a *basis* for a Hilbert space H if for each $f \in H$, there exist unique scalar coefficients $\{c_i\}_{i=1}^m$ such that

$$f = \sum_{i=1}^{m} c_i \, e_i.$$

Definition 2.11. [14] A basis $\{e_i\}_{i=1}^m$ for a Hilbert space H is an *unconditional basis* for H if every permutation σ of $\{e_{\sigma(i)}\}_{i=1}^m$ is a basis of H.

Definition 2.12. A basis $\{e_i\}_{i=1}^m$ for a Hilbert space H is an *orthogonal basis* for H if $\{e_i\}_{i=1}^m$ is an unconditional basis of H and $\langle e_i, e_{i'} \rangle = c_{i,i'} \, \delta_{i,i'}$ for all i and i', where $c_{i,i'} \in \mathbb{R}$ are constants.

Definition 2.13. An orthogonal basis $\{e_i\}_{i=1}^m$ for a Hilbert space H is an *orthonormal basis* for H if $\langle e_i, e_{i'} \rangle = \delta_{i,i'}$ for all i and i'.

Every orthogonal basis can be normalized to obtain an orthonormal basis. In the following, we will use the terms *orthogonal* and *orthonormal* interchangeably unless stated otherwise.

2.2.4 Riesz Bases

Definition 2.14. [98] A sequence of functions $\{f_i\}_{i=1}^m$ is a *Riesz basis* for a Hilbert space H if and only if it is an unconditional basis for H and

$$0 < \inf_i \|f_i\| \leq \sup_i \|f_i\| < \infty. \tag{2.4}$$

Equation 2.4 expresses the fact that a Riesz basis is the image of an orthonormal basis under a bounded invertible operator [98]. It follows from Definitions 2.13 and 2.14 that every orthonormal basis is a Riesz basis.

Theorem 2.3. If $\{f_i\}_{i=1}^m$ is a Riesz basis for a Hilbert space H, then there exists a unique sequence $\{\tilde{f}_i\}_{i=1}^m$ such that

$$f = \sum_{i=1}^m \langle f, \tilde{f}_i \rangle f_i = \sum_{i=1}^m c_i \, f_i \tag{2.5}$$

for all $f \in H$. The sequence $\{\tilde{f}_i\}_{i=1}^m$ is the dual Riesz basis of $\{f_i\}_{i=1}^m$, and Equation 2.5 converges unconditionally for all $f \in H$.

Corollary 2.4. The sequences $\{f_i\}_{i=1}^m$ and $\{\tilde{f}_i\}_{i=1}^m$ are biorthogonal.

Corollary 2.5. The dual of $\{\tilde{f}_i\}_{i=1}^m$ is $\{f_i\}_{i=1}^m$.

Corollary 2.6. The dual of an orthonormal basis $\{f_i\}_{i=1}^m$ is itself.

A proof can be found in the book by Christensen [14]. The sequences $\{f_i\}_{i=1}^m$ and $\{\tilde{f}_i\}_{i=1}^m$ are called the *primary basis* and *dual basis* of H respectively. Given a Riesz basis and its dual, we can obtain the basis function coefficients $\{c_i\}_{i=1}^m$ for any function $f \in H$ by utilizing Theorem 2.3.

2.3 Second Generation Wavelets

2.3.1 Trees and Forests

Definition 2.15. [30] A *forest* is denoted by a quintuple $(\mathcal{F}, g, p, C, <)$, where $\mathcal{F}$ is a countable set of nodes, $g : \mathcal{F} \to \mathbb{Z}$ is a generation function, $p : \mathcal{F} \to \{\mathcal{F}, \emptyset\}$ is a parent function, $C : \mathcal{F} \to p(\mathcal{F})$ is a children function, and $<$ is a partial ordering on $\mathcal{F}$, such that all of the following properties hold for all nodes $\triangle, \triangledown \in \mathcal{F}$:

1. $C(\triangle) = \{\triangledown \in \mathcal{F} \mid p(\triangledown) = \triangle\}$;
2. $0 \leq \#C(\triangle) < \infty$ for each $\triangle \in \mathcal{F}$;
3. If $C(\triangle) = \emptyset$ then $\triangle$ is a *leaf* node;
4. If $\triangledown \in C(\triangle)$, then $g(\triangledown) = 1 + g(\triangle)$;

5. The ordering $<$ linearly orders $C(\triangle)$ for each $\triangle \in \mathcal{F}$;

6. $p^n(\triangle) = \begin{cases} \triangle & \text{if } n = 0; \\ p(p^{n-1}(\triangle)) & \text{if } n \in \mathbb{N}^*; \end{cases}$

7. If $g(\triangle) < g(\triangledown)$ and $p^n(\triangle) = p^m(\triangledown)$ for some $n, m \in \mathbb{N}_0$, then $\triangle < \triangledown$;

8. $\#p(\triangle) \in \{0, 1\}$ for all $\triangle \in \mathcal{F}$;

9. If $p(\triangle) = \emptyset$ then $\triangle$ is a *root* node.

The given partial ordering extends to a linear ordering of the whole forest when each $\mathcal{F}_j$ of $\mathcal{F}$ is ordered linearly, where

$$\mathcal{F}_j = \{\triangle \in \mathcal{F} \mid g(\triangle) = j\}.$$

With the linear ordering we can index the elements of $\mathcal{F}$ with indices $j \in \mathcal{J}$ and $k \in \mathcal{K}(j)$, where $\mathcal{J}$ can be identified with the generation function, and $\mathcal{K}(j)$ is defined by the linear ordering of $\mathcal{F}_j$. A subset $\mathcal{T} \subseteq \mathcal{F}$ is a *tree* if for any $\triangle, \triangledown \in \mathcal{T}$ there are $n, m \in \mathbb{N}_0$ such that $p^n(\triangle) = p^m(\triangledown)$. We will use trees and forests as hierarchical index sets.

2.3.2 Multiresolution Analysis

Definition 2.16. [73] A *multiresolution analysis* $\mathcal{M} = \{V_j \subset L_2 \mid j \in \mathcal{J} \subset \mathbb{Z}\}$ is a sequence of closed subspaces $V_j \subset L_2$ on different scales $j \in \mathcal{J}$, such that

1. $V_j \subset V_{j+1}$;

2. $\bigcup_{j \in \mathcal{J}} V_j$ is dense in L_2;

3. For each $j \in \mathcal{J}$, a Riesz basis of V_j is given by scaling functions $\{\varphi_{j,k} \mid k \in \mathcal{K}(j)\}$.

The set $\mathcal{K}(j)$ is a general index set defined over the scaling functions on level j. Unlike for first generation wavelets, the scaling functions of a multiresolution analysis do not have to be translates and dilates of a mother wavelet function. Although in practice, the scaling functions of a multiresolution analysis usually have similar or identical structure.

Every multiresolution analysis $\mathcal{M}$ has a dual multiresolution analysis $\tilde{\mathcal{M}} = \{\tilde{V}_j \subset L_2 \mid j \in \mathcal{J} \subset \mathbb{Z}\}$, where $\tilde{\mathcal{M}}$ is a sequence of dual spaces $\tilde{V}_j$ spanned by dual scaling functions $\tilde{\varphi}_{j,k}$. The dual scaling basis functions are biorthogonal to the primary scaling basis functions on the same level,

$$\langle \varphi_{j,k}, \tilde{\varphi}_{j,k'} \rangle = \delta_{k,k'}, \quad \text{for } k, k' \in \mathcal{K}(j). \tag{2.6}$$

It follows from Theorem 2.3 that a function $f \in V_{j'}$, for some fixed $j' \in \mathcal{J}$, can be expressed as:

$$f = \sum_{k \in \mathcal{K}(j')} \langle f, \tilde{\varphi}_{j',k} \rangle \, \varphi_{j',k} = \sum_{k \in \mathcal{K}(j')} \lambda_{j',k} \, \varphi_{j',k},$$

where the $\lambda_{j',k}$ are *scaling basis function coefficients*.

2.3.3 Partition

Definition 2.17. [85] Let Σ be a σ-algebra over $X \subseteq \mathbb{R}^n$. A set of measurable subsets $S = \{S_{j,k} \in \Sigma \mid j \in \mathcal{J}, k \in \mathcal{K}(j)\}$ is a *partition* of X if and only if:

1. $\forall j \in \mathcal{J} : \operatorname{clos} \bigcup_{k \in \mathcal{K}(j)} S_{j,k} = X$ and the union is disjoint;
2. $\mathcal{K}(j) \subset \mathcal{K}(j+1)$;
3. $S_{j+1,k} \subset S_{j,k}$;

4. For a fixed $k' \in \mathcal{K}(j')$, $\bigcap_{j>j'} S_{j,k'}$ is a set containing one point $x_{k'} \in X$;

5. $S_{j,k} = \bigcup_{l \in C(S_{j,k})} S_{j+1,l}$.

A partition is a set of nodes $S_{j,k}$ that forms a forest.

2.3.4 Scaling Basis Functions

It follows from the definition of a multiresolution analysis that the scaling basis functions satisfy a *refinement relationship*. More specifically, every scaling function $\varphi_{j,k}$ can be written as a linear combination of the scaling functions $\varphi_{j+1,l}$ at the next finer level:

$$\varphi_{j,k} = \sum_{l \in \mathcal{K}(j+1)} h_{j,k,l}\, \varphi_{j+1,l}. \tag{2.7}$$

The $h_{j,k,l}$ are known as the *scaling basis function filter coefficients*. Similarly, the dual scaling functions $\tilde{\varphi}_{j,k}$ satisfy a refinement relationship with the dual scaling function filter coefficients $\tilde{h}_{j,k,l}$.

In the following, it is assumed that the primary and dual scaling basis function filter coefficients are finite and uniformly bounded. It then follows that the index sets $\mathcal{L}(j,k) = \{l \in \mathcal{K}(j+1) \mid h_{j,k,l} \neq 0\}$ and $\mathcal{K}(j,l) = \{k \in \mathcal{K}(j) \mid h_{j,k,l} \neq 0\}$ are finite for all $j \in \mathcal{J}$ and $k \in \mathcal{K}(j)$. Analogous index sets $\tilde{\mathcal{L}}(j,k)$ and $\tilde{\mathcal{K}}(j,l)$ exist for the dual scaling functions. Unless stated otherwise, l is assumed to run over $\mathcal{L}(j,k)$ or $\tilde{\mathcal{L}}(j,k)$. Likewise, k is assumed to run over $\mathcal{K}(j,l)$ or $\tilde{\mathcal{K}}(j,l)$.

Scaling basis functions can be constructed by using the *cascade algorithm* on a filter sequence $h_{j,k,l}$ and a partition S [85]. First, define a Kronecker sequence $\{\lambda_{j',k} = \delta_{k,k'} \mid k \in \mathcal{K}(j')\}$ for some fixed and arbitrary $j' \in \mathcal{J}$ and $k' \in \mathcal{K}(j')$. Then generate

sequences $\{\lambda_{j,k} \mid k \in \mathcal{K}(j)\}$ for $j > j'$ by recursively applying the equation:

$$\lambda_{j+1,l} = \sum_{k \in \mathcal{K}(j,l)} h_{j,k,l}\ \lambda_{j,k}.$$

Next, define the following function:

$$f^{(j)}_{j',k'} = \sum_{k \in \mathcal{K}(j)} \lambda_{j,k}\ \chi_{S_{j,k}} \qquad \text{for } j \geq j',$$

where $\chi_{S_{j,k}}$ is the characteristic function of $S_{j,k} \in S$. For $j > j'$, the function $f^{(j)}_{j',k'}$ satisfies:

$$f^{(j)}_{j',k'} = \sum_{l} h_{j',k',l}\ f^{(j)}_{j'+1,l}. \tag{2.8}$$

If $\lim_{j\to\infty} f^{(j)}_{j',k'}$ converges to a function in L_2, then it is the scaling function $\varphi_{j',k'}$. Furthermore, if the cascade algorithm converges for all $j' \in \mathcal{J}$ and $k' \in \mathcal{K}(j')$, then the resulting set of scaling functions satisfy the refinement relationship in Equation 2.7. This can be verified by letting j approach infinity in Equation 2.8. The cascade algorithm can also be used to construct the dual scaling functions from a dual filter $\tilde{h}_{j,k,l}$ and the same partition S.

2.3.5 Wavelet Basis Functions

The wavelet basis functions $\psi_{j,k}$ encode the differences between levels j and $j+1$. In other words, the set of wavelet basis functions $\{\psi_{j,m} \mid j \in \mathcal{J}, m \in \mathcal{M}(j)\}$ spans the difference space W_j with $V_j \oplus W_j = V_{j+1}$. The general index set $\mathcal{M}(j) \subset \mathcal{K}(j+1)$ is defined over the wavelet basis functions at level j. Since W_j is a subspace of V_{j+1}, it follows that every wavelet basis function $\psi_{j,m}$ can be written as a linear combination of the scaling functions at the next finer level:

$$\psi_{j,m} = \sum_{l \in \mathcal{K}(j+1)} g_{j,m,l}\ \varphi_{j+1,l}, \tag{2.9}$$

where $g_{j,m,l}$ are the *wavelet basis function filter coefficients*. Similarly, the dual wavelet basis functions $\tilde{\psi}_{j,m}$ can be expressed in terms of the dual scaling functions $\tilde{\varphi}_{j+1,l}$ and dual wavelet basis function filter coefficients $\tilde{g}_{j,m,l}$. In addition, the dual wavelet basis functions span the difference space $\tilde{W}_j$ such that $\tilde{V}_j \oplus \tilde{W}_j = \tilde{V}_{j+1}$. The primary and dual wavelet basis functions are biorthogonal:

$$\langle \psi_{j,m}, \tilde{\psi}_{j',m'} \rangle = \delta_{j,j'} \delta_{m,m'} \quad \text{for} \quad m \in \mathcal{M}(j), m' \in \mathcal{M}(j').$$

In the following, it is assumed that the primary and dual wavelet basis function filter coefficients are finite and uniformly bounded. Hence the index sets $\mathcal{L}(j,m) = \{l \in \mathcal{M}(j+1) \mid g_{j,m,l} \neq 0\}$ and $\mathcal{M}(j,l) = \{m \in \mathcal{M}(j) \mid g_{j,m,l} \neq 0\}$ are finite for all $j \in \mathcal{J}$ and $k \in \mathcal{M}(j)$. Analogous index sets $\tilde{\mathcal{L}}(j,m)$ and $\tilde{\mathcal{M}}(j,l)$ exist for the dual wavelet basis functions. Unless stated otherwise, l is assumed to run over $\mathcal{L}(j,m)$ or $\tilde{\mathcal{L}}(j,m)$. Likewise, m is assumed to run over $\mathcal{M}(j,l)$ or $\tilde{\mathcal{M}}(j,l)$.

2.3.6 Wavelet Bases

Definition 2.18. [47] A *wavelet basis* Ψ is a sequence

$$\Psi = \{\varphi_{0,0}, \psi_{j,m} \mid j \in \mathcal{J}, m \in \mathcal{M}(j)\},$$

where the basis functions provide perfect reconstruction.

The primary basis functions of Ψ are denoted $\hat{\psi}_{j,m} \in \{\varphi_{0,0}, \psi_{j,m}\}$ with $\hat{\psi}_{-1,0} \equiv \varphi_{0,0}$, while the dual basis functions are denoted $\breve{\psi}_{j,m} \in \{\tilde{\varphi}_{0,0}, \tilde{\psi}_{j,m}\}$ with $\breve{\psi}_{-1,0} \equiv \tilde{\varphi}_{0,0}$.

A function $f \in L_2$ can be represented in a wavelet basis as

$$f = \sum_{n \in \mathcal{N}} \langle f, \breve{\psi}_n \rangle \, \hat{\psi}_n = \sum_{n \in \mathcal{N}} \gamma_n \, \hat{\psi}_n,$$

where γ_n are the *wavelet basis function coefficients*, and $\mathcal{N}$ is a general index set defined over all basis functions of Ψ. Note that Ψ forms a forest and $\mathcal{N}$ is a linear ordering on the nodes.

If the primary and dual basis functions coincide, such that $\hat{\psi}_{j,m} = \breve{\psi}_{j,m}$ for all j and k, then Ψ is an *orthogonal* wavelet basis [73]. Therefore, orthogonal wavelet bases are a subset of biorthogonal wavelet bases. It follows from Definition 2.18 that all orthogonal wavelet bases provide perfect reconstruction.

Theorem 2.7. A wavelet basis $\Psi = \{\varphi_{0,0}, \psi_{j,m} \mid j \in \mathcal{J}, m \in \mathcal{M}(j)\}$ is *orthogonal* if and only if the following conditions hold for all $j \in \mathcal{J}$ and $m \in \mathcal{M}(j)$:

1. $\langle \varphi_{j,k}, \varphi_{j,k'} \rangle = \sum_l h_{j,k,l} h_{j,k',l} = \delta_{k,k'}$;
2. $\langle \psi_{j,m}, \psi_{j',m'} \rangle = \sum_l g_{j,m,l} g_{j',m',l} = \delta_{j,j'} \delta_{m,m'}$;
3. $\langle \varphi_{j,k}, \psi_{j',m} \rangle = \sum_l h_{j,k,l} g_{j,m,l} = 0$.

Proof. See [48]. □

2.3.7 Perfect Reconstruction

Theorem 2.8. A wavelet basis Ψ with primary filter coefficients $g_{j,m,l}$, $h_{j,k,l}$ and dual filter coefficients $\tilde{g}_{j,m,l}$, $\tilde{h}_{j,k,l}$ provides *perfect reconstruction* if Ψ is orthogonal and $\sum_k h_{j,k,l}\, \tilde{h}_{j,k,l} + \sum_m g_{j,m,l}\, \tilde{g}_{j,m,l} = 1$ for all $j \in \mathcal{J}$, $k \in \mathcal{K}(j)$ and $m \in M(j)$.

Proof. See [85]. □

2.3.8 Fast Wavelet Transform

The *fast wavelet transform* is a pair of algorithms for transforming between a signal and its representation in a wavelet basis. The *forward transform*, or *analysis*, projects a signal S into a wavelet basis Ψ by the recursive application of:

$$\lambda_{j,k} = \sum_l \tilde{h}_{j,k,l}\ \lambda_{j+1,l} \qquad \text{and} \qquad \gamma_{j,m} = \sum_l \tilde{g}_{j,m,l}\ \lambda_{j+1,l}, \tag{2.10}$$

where $S = \{\lambda_{n,k} \mid k \in \mathcal{K}(n)\}$ is a set of *scaling basis function coefficients* at the finest level n [85]. Given S, the forward transform returns $\{\lambda_{n',k} \mid k \in \mathcal{K}(n')\}$ and $\{\gamma_{j,m} \mid n' \leq j < n, m \in \mathcal{M}(j)\}$.

Correspondingly, the *inverse transform*, or *synthesis*, reconstructs S by the recursive application of:

$$\lambda_{j+1,l} = \sum_k h_{j,k,l}\ \lambda_{j,k} + \sum_m g_{j,m,l}\ \gamma_{j,m}. \tag{2.11}$$

The fast wavelet transform is a linear time algorithm if the primary and dual filters are finite. That is one of the main reasons why the index sets $\mathcal{J}$, $\mathcal{K}$ and $\mathcal{M}$ are required to be uniformly bounded.

2.3.9 Normalization Factors

The following theorem illustrates the need for signal normalization when performing the fast wavelet transform. In particular, the input signal must be normalized in order to obtain the scaling function coefficients at the finest level. Subsequently, the original signal can be recovered by performing the inverse of normalization on the resulting coefficients.

Theorem 2.9. Let $S = \sum_{k \in \mathcal{K}(n)} s_{n,k}\ \chi_{n,k}$ be a discrete signal defined over the domains of a partition at level n, and let Ψ be a Haar-like wavelet basis defined over the same partition with the associated scaling functions $\varphi_{j,k} = \eta_{j,k}\ \chi_{j,k}$, with $j \in \mathcal{J}$ and $k \in \mathcal{K}(j)$, where $\eta_{j,k}$ is a normalization factor. Then the scaling function coefficients of S in Ψ at level n are $\lambda_{n,k} = \frac{s_{n,k}}{\eta_{n,k}}$.

Proof. [47] By the definition of *multiresolution analysis*, the sequence $\{\varphi_{n,k}\}_{k \in \mathcal{K}(n)}$ is a basis of the space over which S is defined. It follows that S can be written as:

$$\begin{aligned} S &= \sum_{k \in \mathcal{K}(j)} \frac{\eta_{n,k}}{\eta_{n,k}}\ s_{n,k}\ \chi_{n,k} \\ &= \sum_{k \in \mathcal{K}(j)} \frac{s_{n,k}}{\eta_{n,k}}\ \varphi_{n,k} \\ \Rightarrow \lambda_{n,k} &= \frac{s_{n,k}}{\eta_{n,k}}. \end{aligned}$$

□

2.3.10 Signal Approximation

Orthogonal bases allow for log-linear time compression that is optimal in the ℓ_2 norm. Thus, orthogonal wavelet bases are potentially well-suited for applications that require efficient signal storage or transmission. The following theorem provides an approximation strategy called the *k-largest approximation*.

Theorem 2.10. Let $S = \sum_{i \in \mathcal{N}} c_i\ f_i$ be a signal in an orthogonal basis Φ for a Hilbert Space X. Let $\Pi = \mathcal{N} \backslash \bar{\mathcal{N}}$, where $\bar{\mathcal{N}} \subset \mathcal{N}$ is an index set of size $\#\bar{\mathcal{N}} = k$ over Φ. Then a k-term approximation $\bar{S} = \sum_{i \in \bar{\mathcal{N}}} c_i\ f_i$ of S is optimal in the ℓ_2 norm if $\{c_i \mid i \in \bar{\mathcal{N}}\}$ is the set of k largest coefficients in $\{c_i \mid i \in \mathcal{N}\}$.

Proof. The ℓ_2 approximation error of $\bar{S}$ with respect to S is

$$\begin{aligned}
\|S - \bar{S}\|_2 &= \left(\int_X |S - \bar{S}|^2 \mathrm{d}x \right)^{1/2} \\
\left(\|S - \bar{S}\|_2 \right)^2 &= \int_X \left(\sum_{i \in \Pi} c_i \, f_i \right)^2 \mathrm{d}x \\
&= \int_X \left(\sum_{i_1 \in \Pi} \gamma_{i_1} \, f_{i_1} \sum_{i_2 \in \Pi} \gamma_{i_2} \, f_{i_2} \right) \mathrm{d}x \\
&= \int_X \left(\sum_{i_1 \in \Pi} \sum_{i_2 \in \Pi} \gamma_{i_1} \, \gamma_{i_2} \, f_{i_1} f_{i_2} \right) \mathrm{d}x \\
&= \sum_{i \in \Pi} c_i^2 \, \langle f_i, f_i \rangle \\
&= \sum_{i \in \Pi} c_i^2. \qquad (2.12)
\end{aligned}$$

The approximation $\bar{S}$ is optimal when $\|S - \bar{S}\|_2$ is minimal. Since $\Pi = \mathcal{N} \setminus \bar{\mathcal{N}}$, it follows from Equation 2.12 that $\|S - \bar{S}\|_2$ is minimal when $\{c_i \mid i \in \bar{\mathcal{N}}\}$ is the set of k largest coefficients in $\{c_i \mid i \in \mathcal{N}\}$. □

Corollary 2.11. The approximation $\bar{S}$ can be obtained from S in $O(n \log n)$, where n is the number of coefficients in $\Gamma = \{c_i \mid i \in \mathcal{N}\}$.

Proof. The set $\bar{\Gamma} = \{c_i \mid i \in \bar{\mathcal{N}}\}$ can be obtained by sorting Γ in descending order to find the k^{th} largest coefficient $\bar{c}_i \in \bar{\Gamma}$. Then replace any coefficients in Γ whose value is less than $\bar{c}_i$ with zero to yield $\bar{\Gamma}$. The worst-case running time for merge sort is $O(n \log n)$, and the time complexity of the other steps is at most $O(n)$. □

Chapter 3

2D SOHO Wavelets

A novel partitioning scheme enables Lessig [47] to develop the 2D SOHO wavelet basis. It is the first spherical Haar wavelet basis for $L_2 \equiv L_2(\mathbb{S}^2, \mathrm{d}\omega)$ that is both orthogonal and symmetric. The standard area measure $\mathrm{d}\omega$ on $\mathbb{S}^2$ is defined as $\mathrm{d}\omega \equiv \mathrm{d}\omega(\theta, \phi) = \sin\theta \mathrm{d}\theta\mathrm{d}\phi$, where $\theta \in [0, \pi]$ and $\phi \in [0, 2\pi]$ are the spherical coordinates of a point on the unit sphere. Only the two-dimensional construction of SOHO will be discussed in this chapter. We will hence omit *2D* whenever no confusion could arise.

3.1 Partition

The SOHO wavelet basis is defined over a partition $\mathcal{P} = \{T_{j,k} \mid j \in \mathcal{J}, k \in \mathcal{K}(j)\}$, where $T_{j,k}$ are spherical triangles called *domains*. The domains $T_{0,k}$ at the coarsest level are obtained by projecting a platonic solid with triangular faces, such as a tetrahedron, octahedron or icosahedron, onto the unit sphere. The domains $T^k_{1,l}$ at the next finer level are formed by subdividing each $T_{0,k}$ into four child domains. Generally, the domains $T^k_{j+1,l}$ at level $j+1$ are formed by subdividing the domains

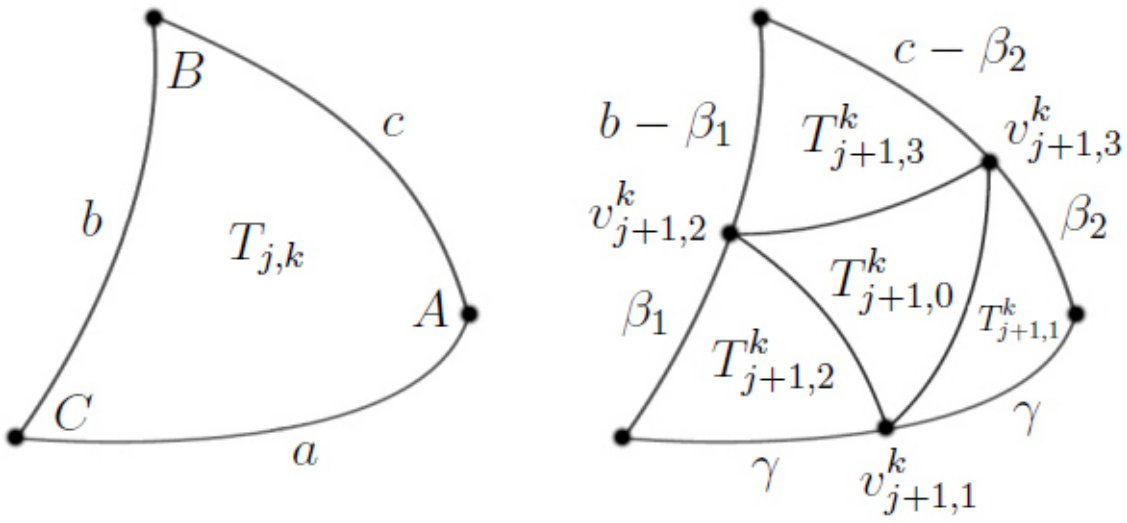

Figure 3.1: Subdivision of a spherical triangle.

$T_{j,k}$ at level j into four child domains. The resulting partition forms a forest, with each domain at the coarsest level being the root node of a tree.

Figure 3.1 illustrates the subdivision of domain $T_{j,k}$. The child domains $T^k_{j+1,l}$ are formed by inserting one new vertex on each great arc of $T_{j,k}$. In addition, the new vertices are positioned such that the three outer child domains $T^k_{j+1,1}$, $T^k_{j+1,2}$ and $T^k_{j+1,3}$ have equal areas. The area isometry restriction is necessary in order to obtain a wavelet basis that is both orthogonal and symmetric.

Definition 3.1. The *characteristic function* $\tau_{j,k} \equiv \tau_{j,k}(\omega)$ of a domain $T_{j,k}$ is

$$\tau_{j,k}(\omega) = \begin{cases} 1 & \text{if } \omega \in T_{j,k} \\ 0 & \text{otherwise.} \end{cases}$$

Definition 3.2. The surface area $\alpha_{j,k}$ of a domain $T_{j,k}$ is

$$\alpha_{j,k}(\omega) = \int_{\mathbb{S}^2} \tau_{j,k}(\omega)\, \mathrm{d}\omega = \int_{T_{j,k}} \mathrm{d}\omega.$$

In general, the equal area constraint cannot be satisfied by simply bisecting each great arc. Instead, we will let one vertex be the geodesic bisector of an arc, and position the remaining two vertices such that $\alpha^k_{j+1,1} = \alpha^k_{j+1,2} = \alpha^k_{j+1,3}$. Without loss of generality, let $v^k_{j+1,1}$ be the geodesic bisector of arc a (Figure 3.1). Then the positions of $v^k_{j+1,2}$ and $v^k_{j+1,3}$ can be determined by solving the system of equations for β_1 and β_1 [47]:

$$\begin{aligned}
\cot\left(\frac{1}{2}E\right) &= \cot(C) + \frac{\cot(\frac{1}{2}\beta_1)\cot(\frac{1}{2}\gamma)}{\sin(C)} \\
\cot\left(\frac{1}{2}E\right) &= \cot(B) + \frac{\cot(\frac{1}{2}\beta_2)\cot(\frac{1}{2}\gamma)}{\sin(B)} \\
\cot\left(\frac{1}{2}E\right) &= \cot(A) + \frac{\cot(\frac{1}{2}b - \frac{1}{2}\beta_1)\cot(\frac{1}{2}c - \frac{1}{2}\beta_2)}{\sin(A)}.
\end{aligned} \tag{3.1}$$

The resulting formulae have been omitted due to their length. It can be shown that exactly one solution exists if the angles A, B and C of the parent domain are labeled consistently (cf. [47]).

Definition 3.3. A spherical Haar wavelet basis is *symmetric* if the basis function coefficients associated with a domain $T_{j,k}$ are invariant to the labeling of the child domains $T^k_{j+1,1}$, $T^k_{j+1,2}$ and $T^k_{j+1,3}$, for an arbitrary but fixed $j \in \mathcal{J}$ and $k \in \mathcal{K}(j)$.

There are six possible ways to reference the three outer child domains with labels $T^k_{j+1,1}$, $T^k_{j+1,2}$ and $T^k_{j+1,3}$. However, a symmetric wavelet basis is invariant under different labels [67]. If a wavelet basis function coefficient γ is associated with a

particular domain $T_{j,k}$, then γ will remain constant even if the child domains of $T_{j,k}$ are labeled differently. In contrast, the wavelet transform would yield different results under different labels if the wavelet basis is not symmetric. Therefore, symmetry is a desirable property in most applications. Another definition of symmetry in terms of linear phase filters exists in the literature (cf. [16]). That notion should not be confused with Definition 3.3 because they are unrelated.

3.2 Scaling Basis Functions

The SOHO scaling basis functions $\varphi_{j,k}$ are constant over their support $T_{j,k}$ so that

$$\varphi_{j,k} = \eta_{j,k}\, \tau_{j,k},$$

where $\eta_{j,k}$ is a normalization factor chosen to satisfy Equation 2.6 [47]. It follows from the SOHO partition scheme that domains $T_{j,k}$ and $T_{j,k'}$ at level $j \in \mathcal{J}$ are disjoint if $k \neq k'$, and so $\langle \varphi_{j,k}, \varphi_{j,k'} \rangle = 0$. Thus Equation 2.6 can be satisfied by ensuring that $\langle \varphi_{j,k}, \varphi_{j,k} \rangle = 1$. By the definition of the inner product on $\mathbb{S}^2$ we have:

$$\begin{aligned}
1 &= \int_{\mathbb{S}^2} \varphi_{j,k}\, \varphi_{j,k}\, \mathrm{d}\omega \\
&= \int_{T_{j,k}} (\eta_{j,k}\tau_{j,k})\, (\eta_{j,k}\tau_{j,k})\, \mathrm{d}\omega \\
&= \eta_{j,k}^2 \int_{T_{j,k}} \mathrm{d}\omega \\
&= \eta_{j,k}^2\, \alpha_{j,k} \\
\Rightarrow \eta_{j,k} &= \frac{1}{\sqrt{\alpha_{j,k}}}.
\end{aligned}$$

Therefore, the SOHO scaling basis function $\varphi_{j,k}$ defined over a domain $T_{j,k}$ is

$$\varphi_{j,k} = \frac{1}{\sqrt{\alpha_{j,k}}}\, \tau_{j,k}. \tag{3.2}$$

The scaling filter coefficients associated with $\varphi_{j,k}$ must satisfy the refinement relationship in Equation 2.7:

$$\varphi_{j,k} = \sum_{l \in \mathcal{L}(j,k)} h_{j,k,l}\, \varphi_{j+1,l}$$
$$\Rightarrow \frac{\tau_{j,k}}{\sqrt{\alpha_{j,k}}} = \sum_{l \in \mathcal{L}(j,k)} h_{j,k,l}\, \frac{\tau^k_{j+1,l}}{\sqrt{\alpha^k_{j+1,l}}}.$$

It follows from the partition that the union of the $\tau^k_{j+1,l}$ is $\tau_{j,k}$. Therefore, the scaling filter coefficient $h_{j,k,l}$ associated with $\varphi_{j,k}$ is

$$h_{j,k,l} = \frac{\sqrt{\alpha^k_{j+1,l}}}{\sqrt{\alpha_{j,k}}}. \tag{3.3}$$

3.3 Wavelet Basis Functions

The SOHO wavelet basis functions $\psi^i_{j,k}$ associated with a domain $T_{j,k}$ are

$$\psi^i_{j,k} = \rho_{j,k} \sum_{l \in \mathcal{K}(j+1)} g^i_{j,k,l}\, \varphi_{j+1,l} \qquad \text{for } i \in \{0,1,2\}, \tag{3.4}$$

where

$$\rho_{j,k} = \frac{1}{\sqrt{9a^2 - 6a + 1}},$$

and the wavelet filter coefficients $g^i_{j,k,l}$ are defined as

$$\begin{aligned} \frac{\sqrt{\alpha^k_{j+1,1}}}{\sqrt{\alpha^k_{j+1,0}}} &= g^0_{j,k,0} = g^1_{j,k,0} = g^2_{j,k,0}; \\ -2a + 1 &= g^0_{j,k,1} = g^1_{j,k,2} = g^2_{j,k,3}; \\ a &= g^0_{j,k,3} = g^0_{j,k,2} = g^1_{j,k,1} = g^1_{j,k,3} = g^2_{j,k,1} = g^2_{j,k,2}, \end{aligned} \tag{3.5}$$

and

$$a = \frac{\alpha^k_{j+1,0} \pm \sqrt{(\alpha^k_{j+1,0})^2 + 3\alpha^k_{j+1,0}\alpha^k_{j+1,1}}}{3\alpha^k_{j+1,0}}. \tag{3.6}$$

In the following, we will briefly describe the construction of the wavelet basis functions. The reader should refer to a thesis by Lessig for a complete derivation (cf. [47]).

The SOHO wavelet basis functions are derived from the wavelet refinement relationship of Equation 2.9. Namely, the wavelet basis functions $\psi_{j,k}$ can be written as a linear combination of the scaling basis functions $\varphi_{j+1,l}$ and the wavelet filter coefficients $g^i_{j,k,l}$. The scaling basis functions can be obtained using Equation 3.2, so the remaining task is to determine the wavelet filter coefficients.

In particular, we want to obtain filter coefficients for a wavelet basis that is both orthogonal and symmetric. Orthogonality can be achieved by deriving filters that satisfy the conditions in Theorem 2.7. Likewise, symmetry can be attained by imposing the equal area constraint on the three outer child domains $T^k_{j+1,1}$, $T^k_{j+1,2}$ and $T^k_{j+1,3}$. Lessig devised a linear system based on these restrictions, and the solution to the system corresponds to the wavelet filter coefficients $g^i_{j,k,l}$ given in Equation 3.5. Note that there are two solutions for Equation 3.6, and therefore two sets of wavelet basis functions can be obtained.

Chapter 4

3D SOHO Wavelets

In the previous chapter, we introduced a wavelet basis over $\mathbb{S}^2$ that is both orthogonal and symmetric. In the following we will generalize the 2D SOHO wavelet basis to obtain a three-dimensional wavelet basis. In particular, the 3D SOHO wavelet basis spans the space $L_2 \equiv L_2(\mathbb{B}^3, \mathrm{d}\omega)$ of functions with finite energy over the ball. The standard volume measure $\mathrm{d}\omega$ on $\mathbb{B}^3$ is defined as $\mathrm{d}\omega \equiv \mathrm{d}\omega(r, \theta, \phi) = \sin\theta \mathrm{d}r\mathrm{d}\theta\mathrm{d}\phi$, where $r \in [0, 1]$, $\theta \in [0, \pi]$ and $\phi \in [0, 2\pi]$ are the spherical coordinates of a point on the unit ball. The following sections will focus on the three-dimensional construction of SOHO. Therefore, we will only use the word *3D* when the context is ambiguous.

4.1 Partition

The SOHO wavelet basis is defined over a partition $\mathcal{P} = \{F_{j,k} \mid j \in \mathcal{J}, k \in \mathcal{K}(j)\}$, where $F_{j,k}$ are spherical frusta called *domains*. A partition $\mathcal{P}$ is generated by recursive subdivision on the unit ball $\mathbb{B}^3 = \{x \in \mathbb{R}^3 \mid \|x\| \leq 1\}$ centered at point O. The domains $F_{0,k}$ at the coarsest level are obtained by a two-step process. First, we generate spherical triangles on the surface S of $\mathbb{B}^3$ by projecting a platonic solid with

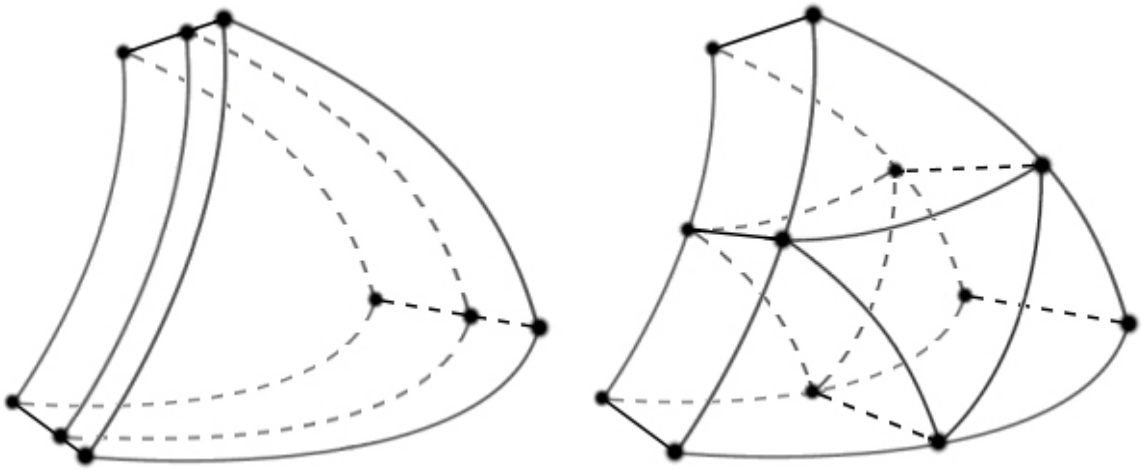

(a) Radial subdivision. (b) Spherical subdivision.

Figure 4.1: Subdivision of spherical frustum $F_{j,k}$.

triangular faces onto S. Next, we insert edges (O, A), (O, B) and (O, C) for each spherical triangle ABC on S. The end result is a set of disjoint spherical tetrahedra $F_{0,k}$, whose union is the unit ball $\mathbb{B}^3$. Geometrically, $\mathbb{B}^3$ can be regarded as a shell whose minimal bounding sphere has a radius of zero. Nevertheless, the volume of shell $\mathbb{B}^3$ and the volume of domains $F_{0,k}$ (Equation 2.3) remain well-defined.

The domains $F^k_{1,l}$ at the next finer level are formed by subdividing each domain $F_{0,k}$ into eight child domains. In general, the domains $F^k_{j+1,l}$ on level $j+1$ are formed by subdividing the domains $F_{j,k}$ on level j into eight child domains. The resulting partition forms a forest of full octrees, with each domain on the coarsest level being the root node of a tree.

Figure 4.1 illustrates the subdivision of domain $F_{j,k}$. The eight child domains $F^k_{j+1,l}$ are formed by dividing $F_{j,k}$ radially into two spherical frusta of equal volumes (Figure 4.1a). In addition, $F_{j,k}$ is spherically divided into four spherical frusta, such that

the outer three frusta have equal volumes (Figure 4.1b). Consequently, there are two child domains $F^k_{j+1,0}$ and $F^k_{j+1,4}$ at the center with equal volumes, along with six outer child domains $F^k_{j+1,1}$, $F^k_{j+1,2}$, $F^k_{j+1,3}$, $F^k_{j+1,5}$, $F^k_{j+1,6}$ and $F^k_{j+1,7}$ with equal volumes.

Definition 4.1. The *characteristic function* $\tau_{j,k} \equiv \tau_{j,k}(\omega)$ of a domain $F_{j,k}$ is

$$\tau_{j,k}(\omega) = \begin{cases} 1 & \text{if } \omega \in F_{j,k} \\ 0 & \text{otherwise.} \end{cases}$$

Definition 4.2. The volume $\alpha_{j,k}$ of a domain $F_{j,k}$ is

$$\alpha_{j,k}(\omega) = \int_{\mathbb{B}^3} \tau_{j,k}(\omega)\, \mathrm{d}\omega = \int_{F_{j,k}} \mathrm{d}\omega.$$

The partition scheme requires that the six outer child domains have equal volumes. Equation 2.1 provides a way to satisfy the equal volume constraint in the radial direction. In general, the equal volume constraint cannot be satisfied in the spherical direction by simply bisecting each great arc in $F_{j,k}$. However, the shell thickness is uniform and thus the quantity $r_2^3 - r_1^3$ in Equation 2.3 is constant for all domains in the same shell. Also, the spherical excess E of $F^k_{j+1,l}$ only depends on the spherical triangle bases of $F^k_{j+1,l}$. Therefore, the equal volume constraint can be satisfied if the bases of the three outer child domains satisfy the equal area constraint.

Definition 4.3. A Haar wavelet basis for $L_2(B^3)$ is *symmetric* if the basis function coefficients associated with a domain $F_{j,k}$ are invariant to the labeling of the outer child domains $F^k_{j+1,1}$, $F^k_{j+1,2}$, $F^k_{j+1,3}$, $F^k_{j+1,5}$, $F^k_{j+1,6}$, $F^k_{j+1,7}$, for a fixed but arbitrary labeling of the center child domains $F^k_{j+1,0}$, $F^k_{j+1,4}$ and a fixed but arbitrary $j \in \mathcal{J}$ and $k \in \mathcal{K}(j)$.

There are $6! = 720$ possible ways to reference the six outer child domains with labels $F^k_{j+1,1}$, $F^k_{j+1,2}$, $F^k_{j+1,3}$, $F^k_{j+1,5}$, $F^k_{j+1,6}$ and $F^k_{j+1,7}$. A symmetric wavelet basis is invariant under any one of the 720 possible labeling schemes. In contrast, the wavelet transform may yield different results under different labels if the wavelet basis is not symmetric. The center child with the larger thickness will be denoted by $F^k_{j+1,0}$ for the remainder of the thesis.

4.2 Scaling Basis Functions

The SOHO scaling basis functions $\varphi_{j,k}$ are constant over their support $F_{j,k}$ so that

$$\varphi_{j,k} = \eta_{j,k}\, \tau_{j,k},$$

where $\eta_{j,k}$ is a normalization factor chosen to satisfy Equation 2.6. It follows from the SOHO partition scheme that domains $F_{j,k}$ and $F_{j,k'}$ at level $j \in \mathcal{J}$ are disjoint if $k \neq k'$, and so $\langle \varphi_{j,k}, \varphi_{j,k'} \rangle = 0$. Thus Equation 2.6 can be satisfied by ensuring that $\langle \varphi_{j,k}, \varphi_{j,k} \rangle = 1$. By the definition of the inner product on $\mathbb{B}^3$ we have:

$$\begin{aligned}
1 &= \int_{\mathbb{B}^3} \varphi_{j,k}\, \varphi_{j,k}\, \mathrm{d}\omega \\
&= \int_{F_{j,k}} (\eta_{j,k}\tau_{j,k})\, (\eta_{j,k}\tau_{j,k})\, \mathrm{d}\omega \\
&= \eta^2_{j,k} \int_{F_{j,k}} \mathrm{d}\omega \\
&= \eta^2_{j,k}\, \alpha_{j,k} \\
\Rightarrow \eta_{j,k} &= \frac{1}{\sqrt{\alpha_{j,k}}}.
\end{aligned}$$

Therefore, the SOHO scaling basis function $\varphi_{j,k}$ defined over a domain $F_{j,k}$ is

$$\varphi_{j,k} = \frac{1}{\sqrt{\alpha_{j,k}}}\, \tau_{j,k}. \tag{4.1}$$

The scaling filter coefficients associated with $\varphi_{j,k}$ must satisfy the refinement relationship in Equation 2.7:

$$\varphi_{j,k} = \sum_{l \in \mathcal{L}(j,k)} h_{j,k,l}\, \varphi_{j+1,l}$$
$$\Rightarrow \frac{\tau_{j,k}}{\sqrt{\alpha_{j,k}}} = \sum_{l \in \mathcal{L}(j,k)} h_{j,k,l}\, \frac{\tau^k_{j+1,l}}{\sqrt{\alpha^k_{j+1,l}}}.$$

It follows from the partition that the union of the $\tau^k_{j+1,l}$ is $\tau_{j,k}$. Therefore, the scaling filter coefficient $h_{j,k,l}$ associated with $\varphi_{j,k}$ is

$$h_{j,k,l} = \frac{\sqrt{\alpha^k_{j+1,l}}}{\sqrt{\alpha_{j,k}}}. \tag{4.2}$$

4.3 Wavelet Basis Functions

In this section, we will derive the 3D SOHO wavelet basis functions. The two-step derivation approach that we employ is very similar to the 2D construction developed by Lessig (cf. [47]). Namely, a semi-orthogonal basis is developed in a first step. Then the semi-orthogonal basis is transformed into an orthogonal and symmetric basis in a second step.

For a Haar-like basis, the wavelet basis functions associated with a domain $F_{j,k}$ are exclusively defined over the eight child domains $F^k_{j+1,l}$. If the wavelet basis functions have a vanishing integral, then $\psi_{j,m}$ can be derived by considering only $F_{j,k}$ and its child domains $F^k_{j+1,l}$, for some fixed but arbitrary $j \in \mathcal{J}$ and $k \in \mathcal{K}(j)$.

To see why $F_{j,k}$ and $F^k_{j+1,l}$ are sufficient, suppose $\psi_{j,m}$ and $\psi_{j',m'}$ are wavelet basis functions with a vanishing integral. If $\psi_{j,m}$ and $\psi_{j',m'}$ are defined over two different

domains on the same level $j = j'$, then their supports are disjoint, and hence they are trivially orthogonal. Hence without loss of generality, let $j < j'$ and suppose $\psi_{j,m}$ and $\psi_{j',m'}$ are associated with domains $F_{j,k}$ and $F_{j',k'}$ respectively. If $F_{j',k'}$ is not a descendent of $F_{j,k}$, then $\psi_{j,m}$ and $\psi_{j',m'}$ are orthogonal, since their supports are once again disjoint. On the other hand if $F_{j',k'}$ is a descendent of $F_{j,k}$, then $\psi_{j,m}$ is constant over the support of $\psi_{j',m'}$ and thus $\langle \psi_{j,k}, \psi_{j',k'} \rangle = 0$. In every case, $\psi_{j,m}$ only depends on $F_{j,k}$ and the child domains $F^k_{j+1,l}$.

Therefore, we will only consider a fixed but arbitrary $F_{j,k}$ and $F^k_{j+1,l}$ in the following derivation of the wavelet basis functions. For the sake of simplicity, we will use the abbreviated notations $\alpha_p \equiv \alpha_{j,k}$ and $\alpha_l \equiv \alpha^k_{j,l}$ to denote the volume of $F_{j,k}$ and $F^k_{j+1,l}$ respectively. Analogous notations will also be used for the characteristic functions.

It follows from Corollary 2.5 that the primary and dual filter coefficients of an orthonormal basis coincide, such that $h_{j,k,l} = \tilde{h}_{j,k,l}$ and $g_{j,m,l} = \tilde{g}_{j,m,l}$ for all $j \in \mathcal{J}$ and $m \in \mathcal{M}(j)$. Therefore, the fast wavelet transforms given by Equations 2.10 and 2.11 can be stated in terms of the filter coefficients $h_{j,k,l}$ and $g_{j,m,l}$.

The synthesis step for $F_{j,k}$ takes the following form in matrix notation

$$\begin{bmatrix} \lambda_{j+1,0} \\ \lambda_{j+1,1} \\ \vdots \\ \lambda_{j+1,7} \end{bmatrix} = \begin{bmatrix} h_{j,k,0} & g^0_{j,k,0} & \cdots & g^6_{j,k,0} \\ h_{j,k,1} & g^0_{j,k,1} & \cdots & g^6_{j,k,1} \\ \vdots & \vdots & \ddots & \vdots \\ h_{j,k,7} & g^0_{j,k,7} & \cdots & g^6_{j,k,7} \end{bmatrix} \begin{bmatrix} \lambda_{j,k} \\ \gamma^0_{j,k} \\ \vdots \\ \gamma^6_{j,k} \end{bmatrix}, \tag{4.3}$$

where $g^i_{j,k,l}$ denotes the l^{th} wavelet filter coefficient associated with the i^{th} wavelet basis function $\psi^i_{j,k}$ defined over $F_{j,k}$, and $h_{j,k,l}$ is the scaling filter coefficient defined

over $F^k_{j,l}$. The 8-by-8 matrix $S_{j,k}$ on the right hand side of Equation 4.3 is called a *synthesis matrix*. The vector $\mathbf{x}$ on the right hand side contains the basis function coefficients associated with $F_{j,k}$. The vector $\mathbf{b}$ on the left hand side contains the scaling basis function coefficients associated with $F^k_{j,l}$.

Similarly, the analysis step for $F^k_{j,l}$ can be expressed as $\mathbf{x} = A_{j,k}\mathbf{b}$, where $A_{j,k}$ is called an *analysis matrix*. Perfect reconstruction requires that $A_{j,k} = S^{-1}_{j,k}$, which is equivalent to $A_{j,k} = S^{\mathrm{T}}_{j,k}$ for an orthonormal basis.

In the first step, we will derive a *semi-orthogonal* basis where the basis functions associated with $F_{j,k}$ is required to satisfy

$$0 = \langle \psi^i_{j,k}, \varphi_{j,k} \rangle \quad \text{for } i \in \{0, \ldots, 6\}. \tag{4.4}$$

For a fixed but arbitrary i, Equation 4.4 can be expanded with the refinement relationship in Equation 2.9:

$$\begin{aligned}
0 &= \langle \psi^i_{j,k}, \varphi_{j,k} \rangle \\
&= \int_{\mathbb{B}^3} \psi^i_{j,k}\ \varphi_{j,k}\, \mathrm{d}\omega \\
&= \int_{\mathbb{B}^3} \left(\sum_{l \in \mathcal{K}(j+1)} \tilde{g}^i_{j,k,l}\ \varphi_{j+1,l} \right)\ \varphi_{j,k}\, \mathrm{d}\omega \\
&= \int_{\mathbb{B}^3} \left(\tilde{g}^i_{j,k,0} \frac{\tau_0}{\sqrt{\alpha_0}} + \ldots + \tilde{g}^i_{j,k,7} \frac{\tau_7}{\sqrt{\alpha_7}} \right) \frac{\tau_p}{\sqrt{\alpha_p}}\, \mathrm{d}\omega \\
&= \frac{\tilde{g}^i_{j,k,0}}{\sqrt{\alpha_0}\sqrt{\alpha_p}} \int_{\mathbb{B}^3} \tau_0\ \tau_p\, \mathrm{d}\omega + \ldots + \frac{\tilde{g}^i_{j,k,7}}{\sqrt{\alpha_7}\sqrt{\alpha_p}} \int_{\mathbb{B}^3} \tau_7\ \tau_p\, \mathrm{d}\omega \\
&= \tilde{g}^i_{j,k,0} \frac{\sqrt{\alpha_0}}{\sqrt{\alpha_p}} + \ldots + \tilde{g}^i_{j,k,7} \frac{\sqrt{\alpha_7}}{\sqrt{\alpha_p}} \\
&= \frac{1}{\sqrt{\alpha_p}} \begin{bmatrix} \sqrt{\alpha_0}, \ldots, \sqrt{\alpha_7} \end{bmatrix} \begin{bmatrix} \tilde{g}^i_{j,k,0} \\ \vdots \\ \tilde{g}^i_{j,k,7} \end{bmatrix}.
\end{aligned} \tag{4.5}$$

Using the result in Equation 4.5, it is easy to verify that a solution to the linear system in Equation 4.4 is

$$\tilde{g}^i_{j,k,l} = \begin{cases} -\frac{\sqrt{\alpha_{i+1}}}{\sqrt{\alpha_0}} & \text{if } l = 0 \\ 1 & \text{if } l = i+1 \\ 0 & \text{otherwise.} \end{cases} \tag{4.6}$$

The wavelet filter coefficients $\tilde{g}^i_{j,k,l}$ in Equation 4.6 form a semi-orthogonal basis. In the second step of the derivation, we will modify the filters to obtain a wavelet basis that is orthogonal and symmetric.

We begin by considering the synthesis matrix $S_{j,k}$ in Equation 4.3. The scaling filter coefficients $h_{j,k,l}$ are obtained using Equation 4.2, so the remaining task is to determine the wavelet filter coefficients $g^i_{j,k,l}$. For this purpose, we let $g^0_{j,k,l} = \tilde{g}^0_{j,k,l}$ and introduce free variables a, b, c and d. Due to the volume isometry restriction, we have $\alpha_0 = \alpha_4$ and $\alpha_1 = \alpha_2 = \alpha_3 = \alpha_5 = \alpha_6 = \alpha_7$.

Then the synthesis matrix in Equation 4.3 can be restated as

$$S_{j,k} = \begin{bmatrix} \frac{\sqrt{\alpha_0}}{\sqrt{\alpha_p}} & -\frac{\sqrt{\alpha_1}}{\sqrt{\alpha_0}} & -\frac{\sqrt{\alpha_1}}{\sqrt{\alpha_0}} & -\frac{\sqrt{\alpha_1}}{\sqrt{\alpha_0}} & -c & -\frac{\sqrt{\alpha_1}}{\sqrt{\alpha_0}} & -\frac{\sqrt{\alpha_1}}{\sqrt{\alpha_0}} & -\frac{\sqrt{\alpha_1}}{\sqrt{\alpha_0}} \\ \frac{\sqrt{\alpha_1}}{\sqrt{\alpha_p}} & b & a & a & a & a & a & a \\ \frac{\sqrt{\alpha_1}}{\sqrt{\alpha_p}} & a & b & a & a & a & a & a \\ \frac{\sqrt{\alpha_1}}{\sqrt{\alpha_p}} & a & a & b & a & a & a & a \\ \frac{\sqrt{\alpha_0}}{\sqrt{\alpha_p}} & a & a & a & d & a & a & a \\ \frac{\sqrt{\alpha_1}}{\sqrt{\alpha_p}} & a & a & a & a & b & a & a \\ \frac{\sqrt{\alpha_1}}{\sqrt{\alpha_p}} & a & a & a & a & a & b & a \\ \frac{\sqrt{\alpha_1}}{\sqrt{\alpha_p}} & a & a & a & a & a & a & b \end{bmatrix}.$$

The wavelet filter coefficients in $S_{j,k}$ can be obtained by enforcing three conditions:

$$0 = \langle \psi^i_{j,k}, \varphi_{j,k} \rangle \qquad \text{for } i \in \{0, \ldots, 6\} \tag{4.7a}$$

$$0 = \langle \psi^i_{j,k}, \psi^{i'}_{j,k} \rangle \qquad \text{for } i, i' \in \{0, \ldots, 6\} \text{ and } i \neq i' \tag{4.7b}$$

$$0 = \int_{\mathbb{B}^3} \psi^i_{j,k} \, \mathrm{d}\omega \qquad \text{for } i \in \{0, \ldots, 6\}. \tag{4.7c}$$

Equation 4.7a maintains semi-orthogonality, while Equations 4.7b and 4.7c enforce orthogonality and vanishing integral of the wavelet basis functions respectively. Symmetry is established implicitly by the equal volume restriction of the partition.

Equations 4.7a, 4.7b and 4.7c can be expanded using the elements in matrix $S_{j,k}$. The result is a linear system of four unique equations

$$\begin{aligned}
0 &= 5a^2 + 2ab + \frac{\alpha_1}{\alpha_0} \\
0 &= 5a^2 + (b + d)\, a + \frac{\sqrt{\alpha_1}}{\sqrt{\alpha_0}}\, c \\
0 &= -\sqrt{\alpha_1} + \sqrt{\alpha_1}\, b + (5\sqrt{\alpha_1} + \sqrt{\alpha_0})\, a \\
0 &= -\sqrt{\alpha_0}\, c + 6\sqrt{\alpha_1}\, a + \sqrt{\alpha_0}\, d.
\end{aligned}$$

Solving the linear system for a, b, c and d gives the wavelet filter coefficients $g^i_{j,k,l}$. Lastly, an orthonormal basis can be obtained by normalizing the wavelet basis func-

tions $\psi^i_{j,k}$ with a normalization constant $\rho^i_{j,k}$ so that

$$\begin{aligned} 1 &= \langle \psi^i_{j,k}, \psi^i_{j,k} \rangle \\ &= \int_{\mathbb{B}^3} \sum_l \rho^i_{j,k}\, g^i_{j,l}\, \varphi^k_{j+1,l} \sum_{l'} \rho^i_{j,k}\, g^i_{j,l'}\, \varphi^k_{j+1,l'}\, \mathrm{d}\omega \\ &= \sum_l \left(\rho^i_{j,k}\right)^2 \left(g^i_{j,l}\right)^2 \int_{\mathbb{B}^3} \left(\varphi^k_{j+1,l}\right)^2 \mathrm{d}\omega \\ &= \left(\rho^i_{j,k}\right)^2 \sum_l \left(g^i_{j,l}\right)^2 \\ \Rightarrow \rho^i_{j,k} &= \frac{1}{\sqrt{\sum_l \left(g^i_{j,l}\right)^2}}. \end{aligned}$$

Therefore, the SOHO wavelet basis functions $\psi^i_{j,k}$ associated with a domain $F_{j,k}$ are

$$\psi^i_{j,k} = \rho^i_{j,k} \sum_{l \in \mathcal{K}(j+1)} g^i_{j,k,l}\, \varphi_{j+1,l} \qquad \text{for } i \in \{0, \ldots, 6\}, \tag{4.8}$$

where

$$\rho^i_{j,k} = \begin{cases} (c^2 + 6a^2 + d^2)^{-1/2} & \text{if } i = 4 \\ (\Delta^2 + 6a^2 + b^2)^{-1/2} & \text{otherwise,} \end{cases}$$

and

$$g^i_{j,k,l} = \begin{cases} -\frac{\sqrt{\alpha_1}}{\sqrt{\alpha_0}} & \text{if } l = 0 \text{ and } i \neq 4 \\ -c & \text{if } l = 0 \text{ and } i = 4 \\ b & \text{if } l = i + 1 \text{ and } i \neq 4 \\ d & \text{if } l = i + 1 \text{ and } i = 4 \\ a & \text{otherwise,} \end{cases} \tag{4.9}$$

and

$$
\begin{aligned}
a &= \frac{\sqrt{\alpha_1}\left(1 \pm \sqrt{1 + 5\Delta^2 + 2\Delta}\right)}{5\sqrt{\alpha_1} + 2\sqrt{\alpha_0}} \\
b &= 1 - \left(5 + \frac{1}{\Delta}\right) a \\
c &= \frac{a\left(6\sqrt{\alpha_0}\alpha_1 a + \sqrt{\alpha_0}^3 a - \alpha_0\sqrt{\alpha_1}\right)}{\sqrt{\alpha_0}\alpha_1 + \alpha_0\sqrt{\alpha_1}a} \\
d &= \frac{a\left(\sqrt{\alpha_0}^3 a - \alpha_0\sqrt{\alpha_1} - 6\sqrt{\alpha_1}^3\right)}{\sqrt{\alpha_0}\alpha_1 + \alpha_0\sqrt{\alpha_1}a} \\
\Delta &= \sqrt{\frac{\alpha_1}{\alpha_0}}.
\end{aligned}
\tag{4.10}
$$

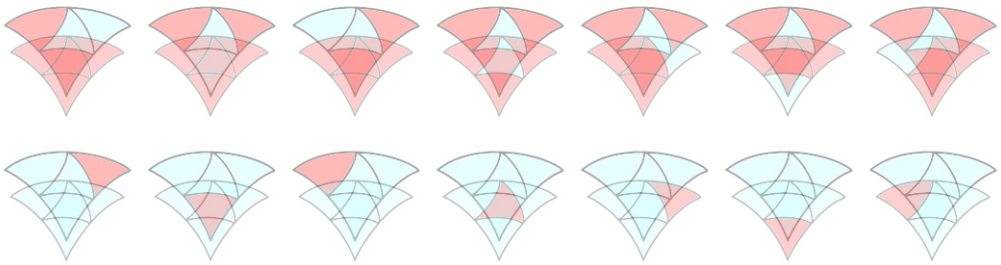

Figure 4.2: The seven wavelet basis functions defined over a domain on the coarsest level. The top row shows the basis functions associated with parameter a obtained by addition in Equation 4.10, while the bottom row shows the basis functions associated with subtraction. Child domains are shown as spherical triangles. Red and blue regions indicate positive and negative wavelet filter coefficients respectively.

Chapter 5

Experiments

5.1 Introduction

Orthogonality, symmetry and other theoretical properties of SOHO were presented in the previous chapters. Whether or not such properties translate into good performance in practice will be investigated in this chapter. We conducted a variety of experiments to evaluate 3D SOHO, in terms of its ability to represent and to approximate different types of signals. The objective of this chapter is to provide general insights that are relevant to a wide range of applications.

We begin the next section by defining *performance* and how it is measured (Section 5.2.1). Next, the signals (Section 5.2.2) and bases (Section 5.2.3) that were selected for experimentation are presented, along with the rationale behind each selection. The methodology section concludes with a detailed account of the implementation and experimental setup (Section 5.2.4). Results are presented in Section 5.3, followed by an analysis and interpretation of the data (Section 5.4).

5.2 Methods

5.2.1 Error Norms

The performance of 3D SOHO is quantitatively measured in terms of the ℓ_1, ℓ_2 and ℓ_∞ norms. We selected the ℓ_2 norm because it is the standard measure for the space $L_2(\mathbb{B}^3, d\omega)$. The ℓ_2 norm is also commonly used in the literature, thereby providing a basis for comparison. However, it has been argued that the ℓ_1 norm is a better quantitative measure for the perceived image quality than the ℓ_2 norm [22]. Furthermore, the ℓ_∞ norm is a useful measure for applications with a maximum error tolerance requirement. Therefore, we also employed the ℓ_1 and ℓ_∞ norms in our experiments.

Resampling Error

Source signals can assume various spatial parameterizations and sampling rates. Therefore, it is often necessary to resample a source signal prior to analysis, so that the resampled signal is constant over the support of each domain on the finest level. *Resampling error* is the difference between a source signal and a resampled signal, and it can be estimated using the Monte Carlo method given by Definition 5.1.

Definition 5.1. The ℓ_p *resampling error* E_p of a resampled signal $\bar{S}$ with respect to a source signal S is

$$E_p = \left(\int_{\mathbb{B}^3} \mid S(x) - \bar{S}(x) \mid^p \mathrm{d}x \right)^{1/p} \approx \frac{V}{n} \sum_{i=1}^{n} \| S(x_i) - \bar{S}(x_i) \|_p, \tag{5.1}$$

where V is the volume of the unit ball, and n is the number of random samples.

The concept of resampling error is not unique to 3D SOHO partitions. For instance, a source signal can be resampled to obtain a volume of voxels. Then the resampling error can be computed using Equation 5.1, and by replacing V with the overall volume of the voxels.

Approximation Error

Approximation error is the difference between a resampled signal and an approximated signal. Unlike resampling error, we can determine the exact approximation error by comparing each domain in a resampled signal with the corresponding domain in its approximation.

Definition 5.2. The ℓ_p *approximation error* E_p of an approximation $\bar{S}$ with respect to a resampled signal S is

$$E_p = \|S - \bar{S}\|_p.$$

5.2.2 Signals

Four different types of source signals were used in the experiments. Volumetric data sets were selected from the field of medical imaging, geoscience and computer graphics. The aim is to evaluate SOHO on a variety of real-world signals. In this section, we will describe each of the source signals in detail.

CBCT

Cone Beam Computed Tomography (CBCT) is an imaging technique utilizing x-rays. An object is placed on the turntable between the x-ray source and the detector panel.

The turntable rotates the object about a fixed vertical axis for one full revolution, while a series of two-dimensional x-ray images are captured [13]. These x-ray images are called *projections*, and together they form a *projection set*.

A process known as *backprojection* is used to reconstruct the 3D signal given a projection set. Intuitively, backprojection is similar to ray tracing except it is done in reverse. The signal at point $\bar{p}$ is determined by casting a ray $\vec{r}$ from the x-ray source $\bar{s}$ through $\bar{p}$, until $\vec{r}$ intersects with the detector panel at some pixel $\bar{q}$. Then the signal at $\bar{p}$ is the summation of pixels $\bar{q}$, over all projections in the projection set. In essence, the values at $\bar{q}$ represent the attenuation of the x-ray as it travels through the object along $\vec{r}$.

Projections are made while the object rotates on a turntable. Therefore pixel $\bar{q}$ is generally different for each projection, unless $\bar{p}$ is on the axis of rotation. After a single rotation, each point $\bar{p}$ in the object will map to a unique series of pixels on the detector. Also note that $\bar{p}$ is not the only point that will map to pixel $\bar{q}$ in a particular projection. In fact, every point $\bar{p}$ along ray $\vec{r}$ is given the value at $\bar{q}$ even if $\bar{p}$ is located in the empty space outside of the object. Consequently, artifacts appear in the reconstruction as "smears" (Figure 5.1b).

A source signal was obtained from a medical CBCT projection set of a plastic mannequin head (Figure 5.1a). The projection set consists of 320 projections taken at roughly every 1.14 degrees. Physical pixel pitch is approximately 0.2 millimeters in both dimensions. Each projection is 512 pixels in width, 384 pixels in height and 4 bytes per pixel.

MRI

Magnetic Resonance Imaging (MRI) is an imaging technique that uses a magnetic field and radio frequency (RF) pulse to induce nuclear magnetic resonance (NMR) on protons [95]. The magnetic field causes the magnetic moments of the protons to align with the direction of the magnetic field. An RF pulse is then briefly activated, causing the protons to alter their alignment relative to the magnetic field. When the RF pulse is deactivated, the protons release energy as they return to their original alignment. The resulting signal can be detected by a scanner, and used to construct a volume.

A simulated brain MRI volume was acquired from a web interface known as *BrainWeb* [17]. The MRI volume was employed as one of the source signals in our experiments (Figure 5.2). BrainWeb provides access to a brain MRI simulator that can generate realistic volumes based on input parameters, including noise level, slice thickness and intensity non-uniformity level. Volumes generated by BrainWeb can serve as ground truth for evaluating quantitative brain image analysis methods, such as tissue classification algorithms.

The simulator begins with a digital brain phantom based on real MRI scans. The phantom consists of ten volumetric data sets that define spatial distribution and ratio for gray matter, white matter, muscle, skin and other types of tissues [18]. Bloch equations are then used to simulate NMR signal production and to model the imaging process [45, 46].

The brain MRI volume that was used in our experiments consists of 217 slices that encompasses the entire brain, starting from the top of the scalp to the base of the

foramen magnum. The volume was generated with uniform intensity, without any noise and without any multiple-sclerosis lesions. Each T1-weighted slice is 181 pixels in width, 181 pixels in height and 1 byte per pixel. Physical voxel pitch is one millimeter wide in each dimension.

SLIMCAT

SLIMCAT is a three-dimensional chemical transport model that is widely used in atmospheric chemistry research [12]. The model is initialized with the measured concentration of one or more chemical species in the Earth's atmosphere. SLIMCAT then simulates the biogeochemical cycle, such as flow and chemical production.

The *SLIMCAT Reference Atmosphere* served as one of the source signals in our experiments (Figure 5.3). Atmospheric measurements were made over a period of twelve months, starting from October of 1991. A volume was generated for each month, although we only utilized the data set for the month of September.

The SLIMCAT Reference Atmosphere spans the entire globe, with a spatial resolution of 7.5 degrees longitudinally, 5 degrees latitudinally and 18 levels vertically. The lowest level is at ground-level, while the highest level is centered at 10 hectopascals. The SLIMCAT Reference Atmosphere models temperature, pressure and distribution fields for 37 chemical species. However, we only employed the temperature data in our experiments.

Perlin Noise

Textures are commonly stored in the form of a bitmap, or a 2D array of pixels. Procedural textures, on the other hand, are represented using algorithms and mathematical expressions. In this section we will informally describe a type of procedural texture called *Perlin noise*. Refer to the works of Perlin et al. [68, 69] for a complete definition.

Perlin noise is a function that generates pseudorandom noise. A Perlin function is a mapping $\mathbb{R}^3 \to \mathbb{R}$ that is generated from a rectangular lattice in $\mathbb{R}^3$. The lattice grid points are evenly spaced in each dimension, and every point is assigned a random unit gradient vector. For any point $\bar{p} \in \mathbb{R}^3$, there are eight grid points surrounding it called the *neighbors* of $\bar{p}$.

The signal at point $\bar{p} \in \mathbb{R}^3$ is determined by the gradient vectors of its neighbors. More specifically, $G(\bar{q}) \cdot (\bar{p} - \bar{q})$ is computed for each neighbor $\bar{q}$ of $\bar{p}$, where $G(\bar{q})$ is the gradient vector assigned to $\bar{q}$. The signal at $\bar{p}$ is interpolated from these dot products, using an S-shaped cross-fade function to weight the interpolant in each dimension.

Perlin noise is *pseudorandom* because it gives the appearance of randomness, although the function itself is deterministic. The function will always generate the same noise, as long as the same gradient vectors are used. In addition, the spatial frequency of Perlin noise is bandlimited and invariant under translation.

Given a Perlin function defined over $\mathbb{R}^3$, we can generate a signal in $\mathbb{B}^3$ by intersecting a ball with $\mathbb{R}^3$. Essentially, the signal is "sculpted" from a virtual block of texture. The signal frequency is inversely proportional to the amount of space between grid points in the lattice.

Two different source signals were generated for our experiments using Perlin noise functions. Perlin Noise A was generated using one gradient per unit length in all three dimensions, while fifty gradients per unit length were used for Perlin Noise B (Figure 5.4).

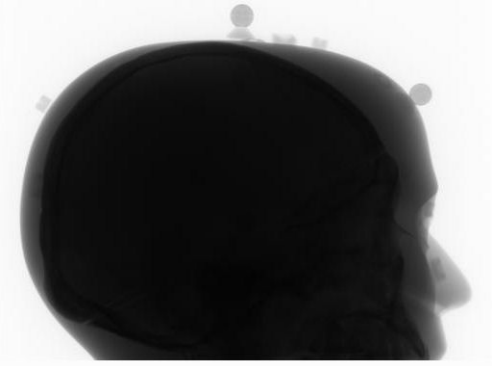

(a) A single sagittal projection.

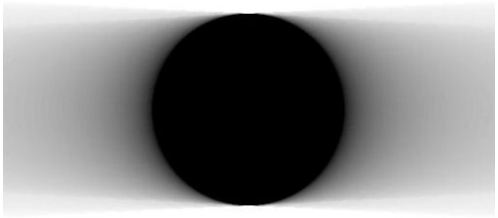

(b) A slice taken from the reconstruction of a solid sphere. Smearing is clearly visible around the sphere.

Figure 5.1: CBCT Projections.

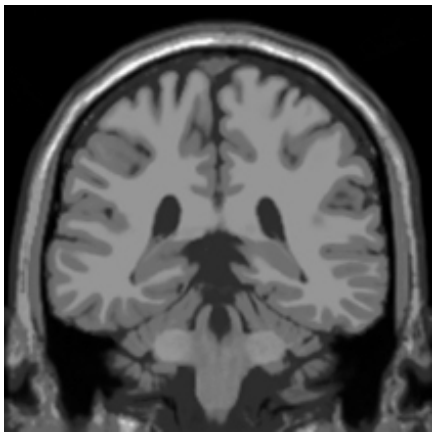

(a) Coronal slice.

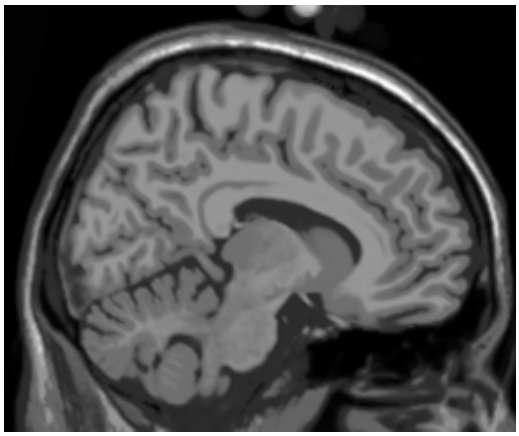

(b) Sagittal slice.

Figure 5.2: Brain MRI Slices.

Figure 5.3: SLIMCAT Reference Atmosphere.

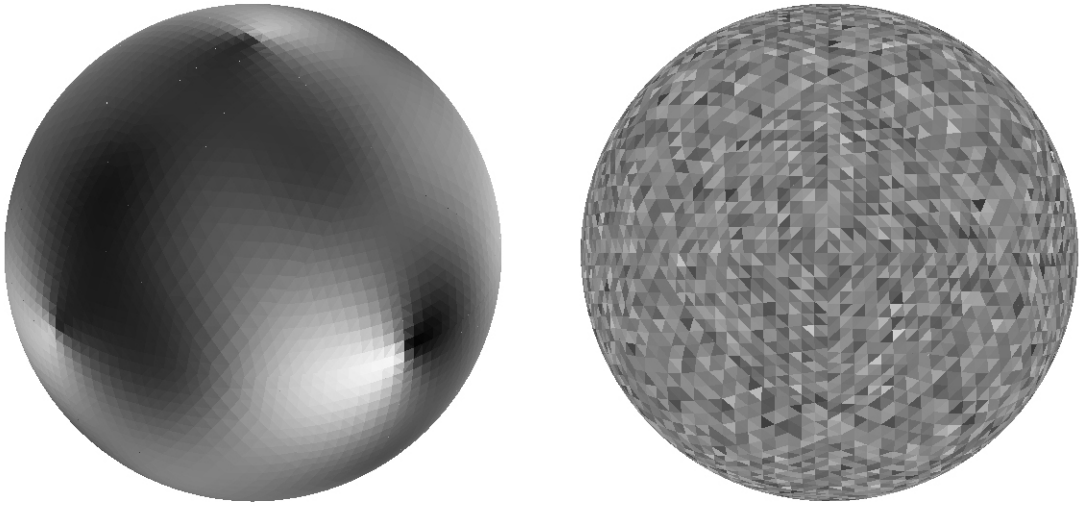

(a) Perlin Noise A.

(b) Perlin Noise B.

Figure 5.4: Perlin noise.

5.2.3 Bases

We compared the approximation performance of 3D SOHO against that of three other bases. The well-know Haar basis over 3D Euclidean space [82] was selected for the purpose of comparing SOHO against another orthonormal wavelet basis. Haar approximations were generated by applying the Haar wavelet transform on each dimension of a rectangular volume, followed by the k-largest approximation strategy.

Lossy data compression algorithms based on discrete cosine transform (DCT) have been used in MP3, JPEG and other popular digital media encoding formats. Likewise, DCT has also been applied to volumetric compression [96]. We decided to compare SOHO against DCT due to its widespread adoption. DCT approximations were generated by employing DCT-II on each dimension of a rectangular volume, followed by the k-largest approximation strategy.

Rectangular cuboid is the most common geometry for representing volumetric data. That is one of the main reasons why the Haar basis and DCT was chosen for our experiments. However, we also wanted to compare SOHO against another spherical solid basis. Therefore, we chose the angular portion of an orthogonal set of solutions to Laplace's equation known as *Solid Harmonics* [89]. In fact, Spherical Harmonics are the restriction of Solid Harmonics to the surface of the unit sphere. Approximations of different fidelities were generated by varying the number of bands in the regular Solid Harmonic projections.

5.2.4 Experimental Setup

Experiments were conducted using MATLAB version 7.6 on a 64-bit Linux based operating system. The workload was divided among nine independent computing nodes,

with 4.2TB of shared storage. Each node has two 3.8GHz Intel Xeon processors and 4GB of main memory. Computations were performed exclusively in double precision. This section will highlight the implementation details and design decisions that are important for reproducibility.

Partitions

As seen in Section 4.1, a partition can be mathematically expressed in terms of a forest. Although a tree data structure is a natural choice for implementing a partition, we decided to use vectors for efficiency reasons. A partition with n levels can be represented by a forest of full octrees with height $n-1$. The forest topology is fixed, and so it can be stored as a vector rather than a hierarchical tree structure. As a result, node access can be achieved in constant time, rather than logarithmic time required by tree traversal. Vectorized operations are also generally faster than scalar operations in MATLAB [52].

Controlled variables were kept constant for all experiments in order to maximize comparability. More specifically, a standard partition was constructed from an octahedron and subdivided into 6 levels. Hence the partition consisted of 32 shells and 8^6 domains on the finest level. In addition, the equal volume constraint was enforced for all domain subdivisions. By default, the parameter "a" in Equation 4.10 was computed using subtraction rather than addition. Lastly, $8^6 \times 10 = 2,621,440$ random samples were used for signal resampling, and to compute resampling errors. That is equivalent to 10 random samples per domain on the finest level of a standard partition.

Volumes

Rectangular volumes were needed to evaluate the approximation performance of the Haar basis and DCT. Precautions were taken in order to avoid biases, either toward voxel volumes or spherical volumes. For instance, voxels volumes were generated such that the number of voxels and its overall volume was equivalent to the number of domains and the overall volume of a standard SOHO partition, respectively. Hence a standard volume comprised of 64 isotropic voxels in each dimension, and a total volume of $4\pi/3$. Likewise, 10 random samples per voxel were used for signal resampling, and to compute resampling errors.

Approximations

Approximations in DCT, Haar and SOHO were generated using at most $8^6 = 262,144$ basis function coefficients. However, Solid Harmonic approximations were limited to 50 bands due to memory limitations in MATLAB. Therefore, one set of experiments compared DCT, Haar and SOHO with up to 8^6 coefficients, while another set of experiments included Solid Harmonic and utilized up to 50^2 coefficients.

5.3 Results

Data were gathered from 10 different experiments on four different types of signals. The results are summarized in the following graphs. Some experiments have been omitted because the results are almost identical to the ones that are shown in this section.

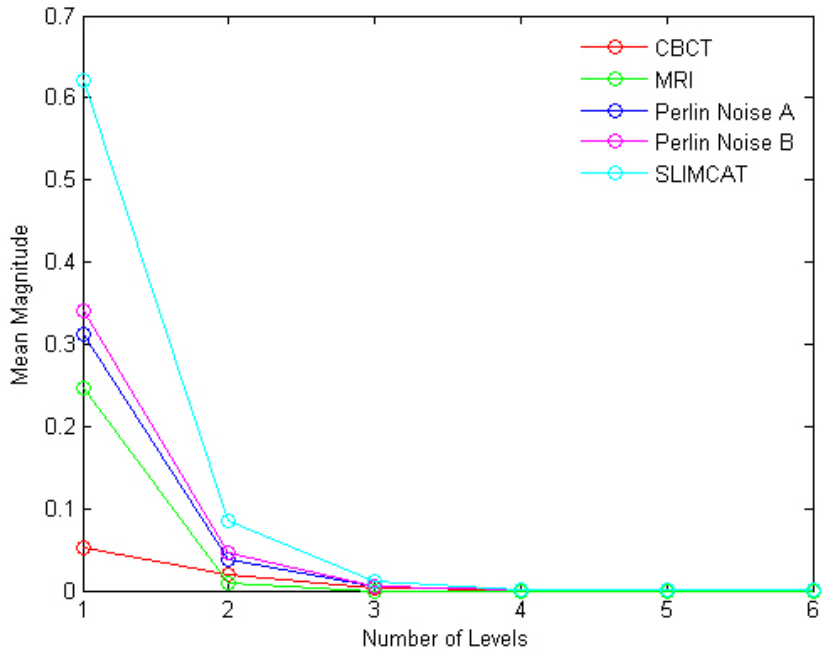

Figure 5.5: Decay of SOHO wavelet basis function coefficients with increasing levels.

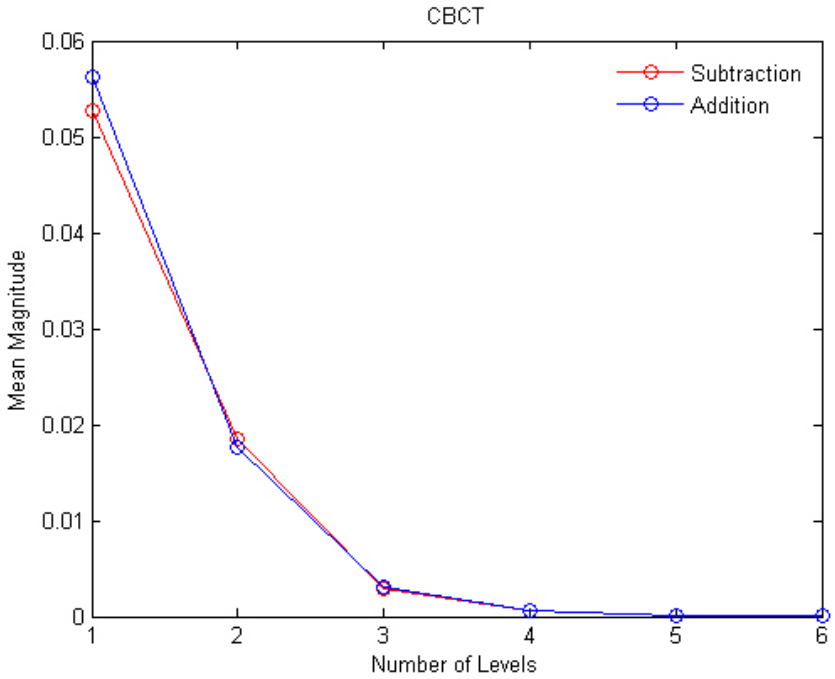

Figure 5.6: Decay of SOHO wavelet basis function coefficients with increasing levels, for the two possible solutions of Equation 4.10. Other signals produce similar graphs.

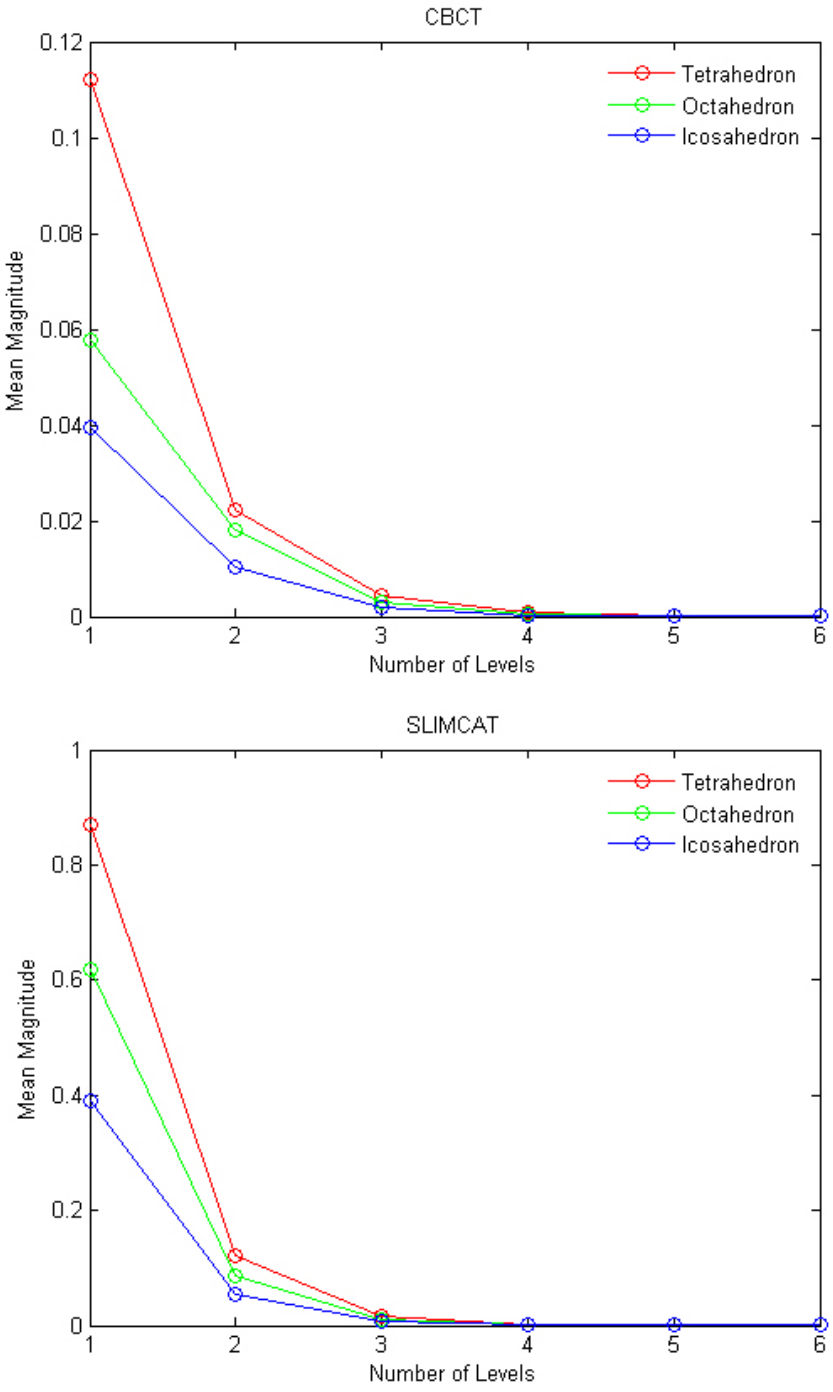

Figure 5.7: Decay of SOHO wavelet basis function coefficients with increasing levels, for the three possible choices of platonic solids. Other signals produce similar graphs.

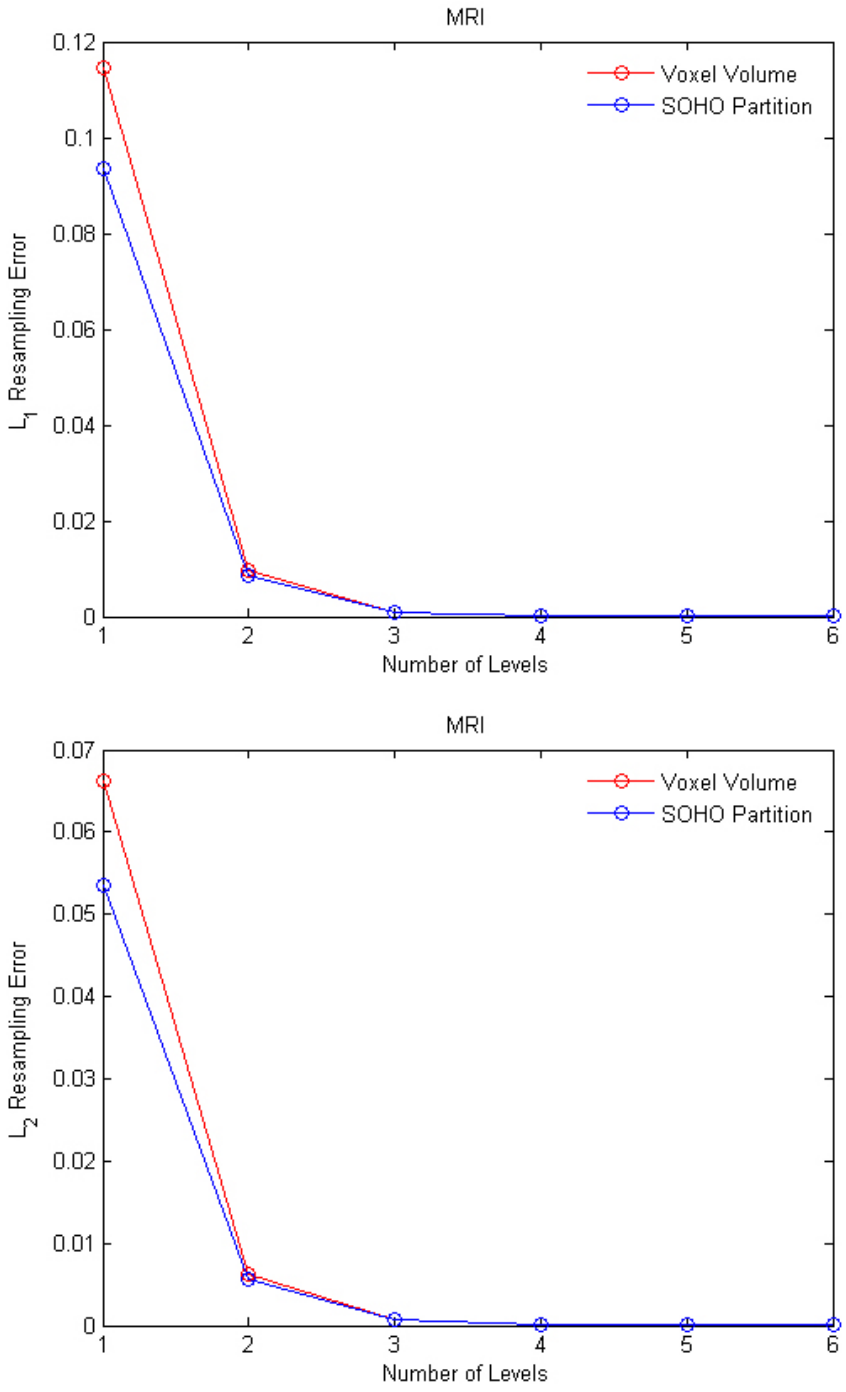

Figure 5.8: Comparison of resampling performance between SOHO partitions and voxel volumes. Other signals produce similar graphs.

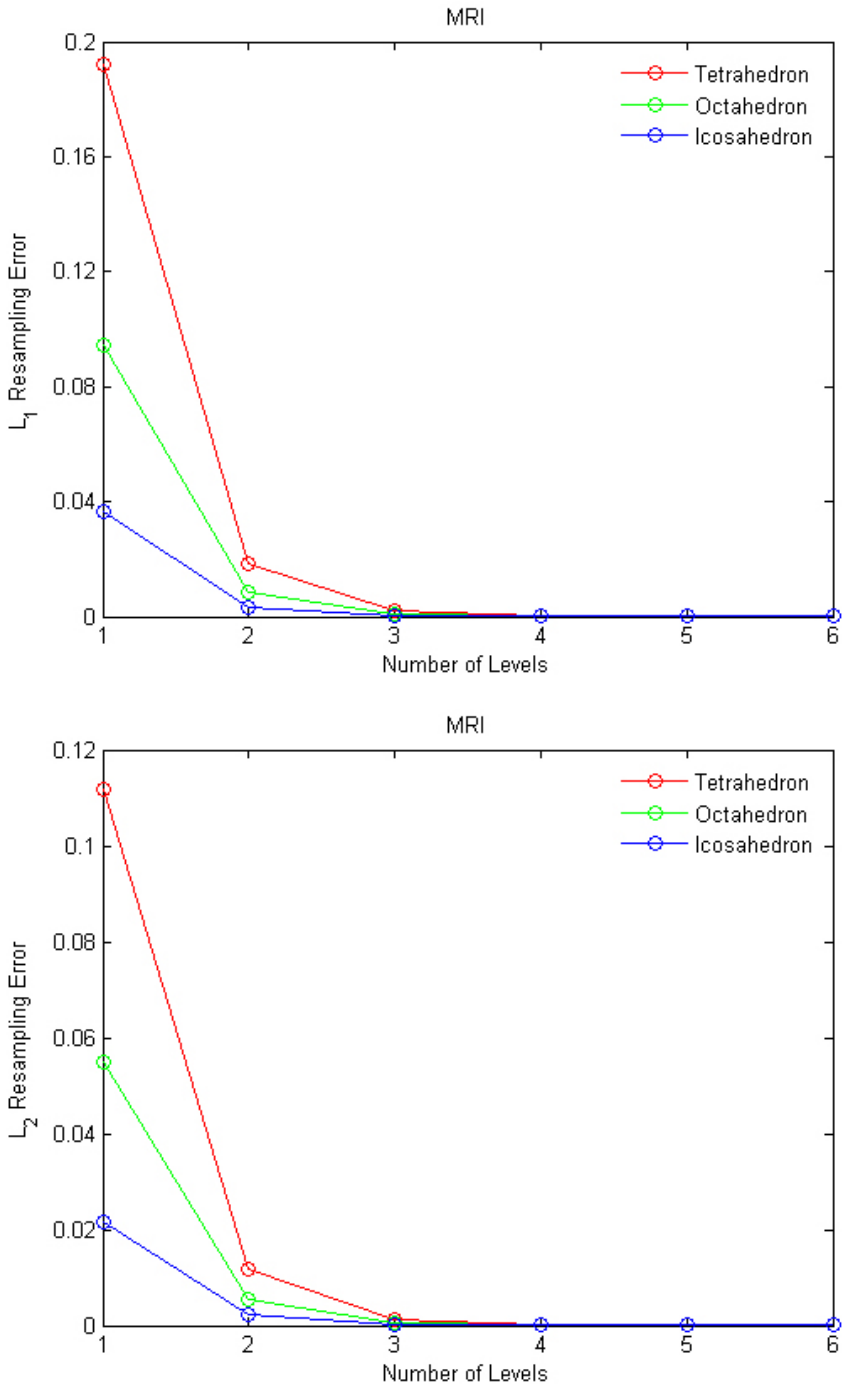

Figure 5.9: Resampling error of SOHO partitions with different number of levels, for the three possible choices of platonic solids. Other signals produce similar graphs.

Figure 5.10: Comparison of approximation performance on CBCT.

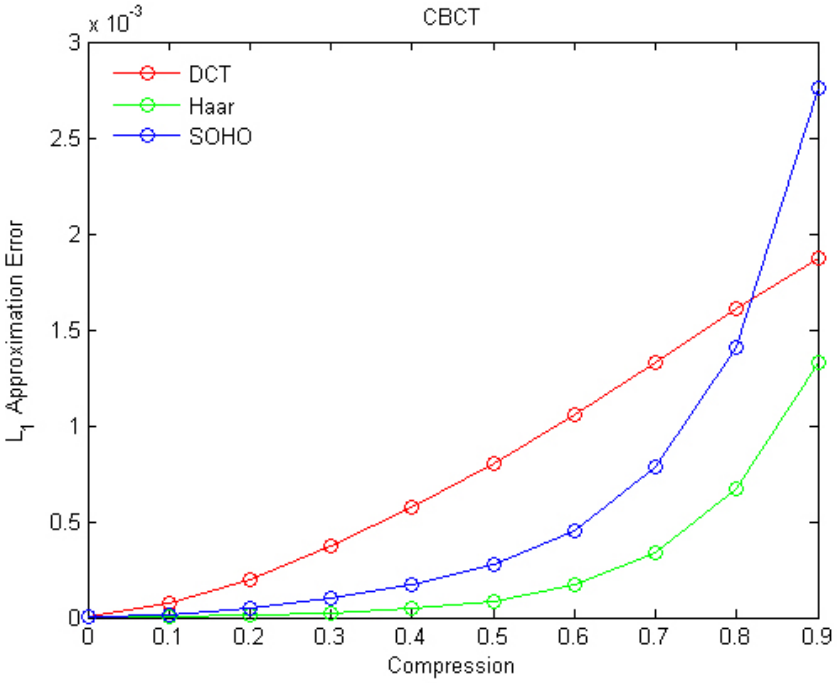

(a)

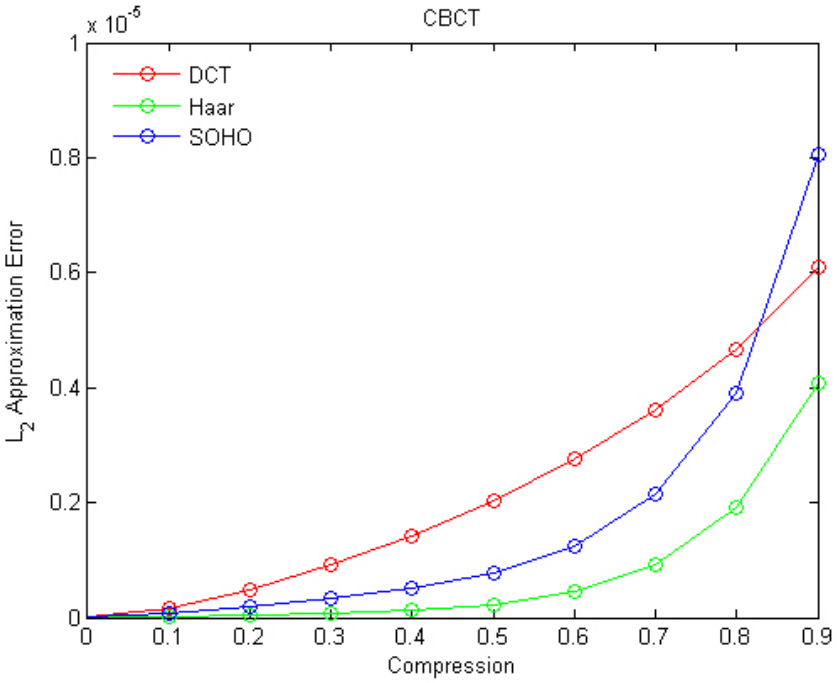

(b)

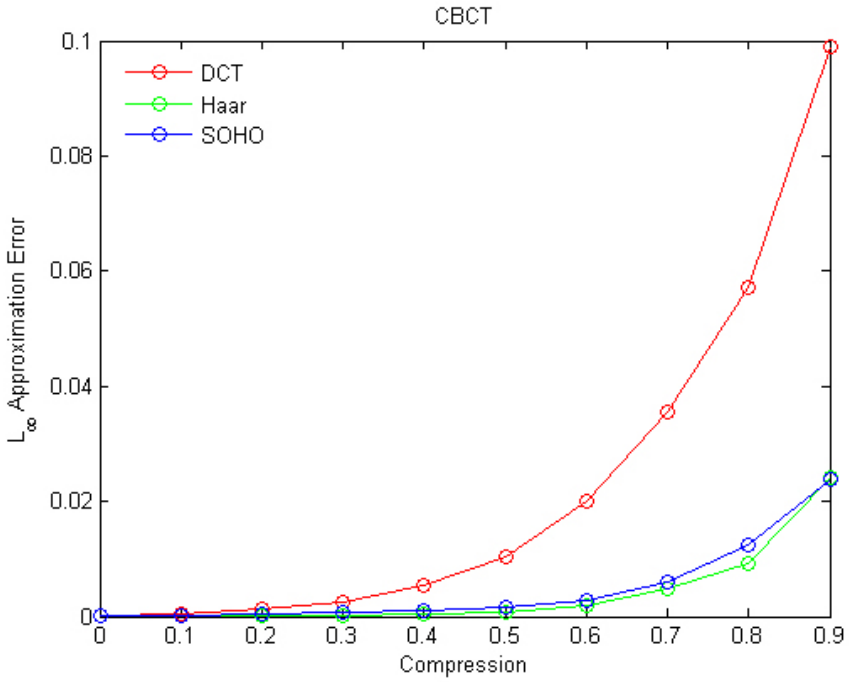
CBCT
DCT
Haar
SOHO
L_∞ Approximation Error
Compression
0
0.02
0.04
0.06
0.08
0.1
0.1
0.2
0.3
0.4
0.5
0.6
0.7
0.8
0.9

(c)

Figure 5.11: Comparison of approximation performance on MRI.

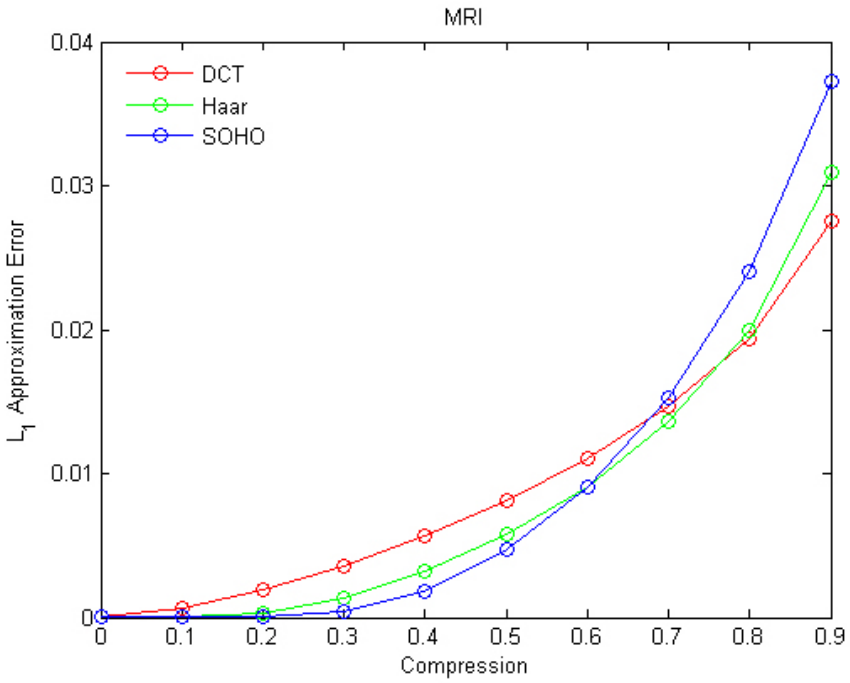

(a)

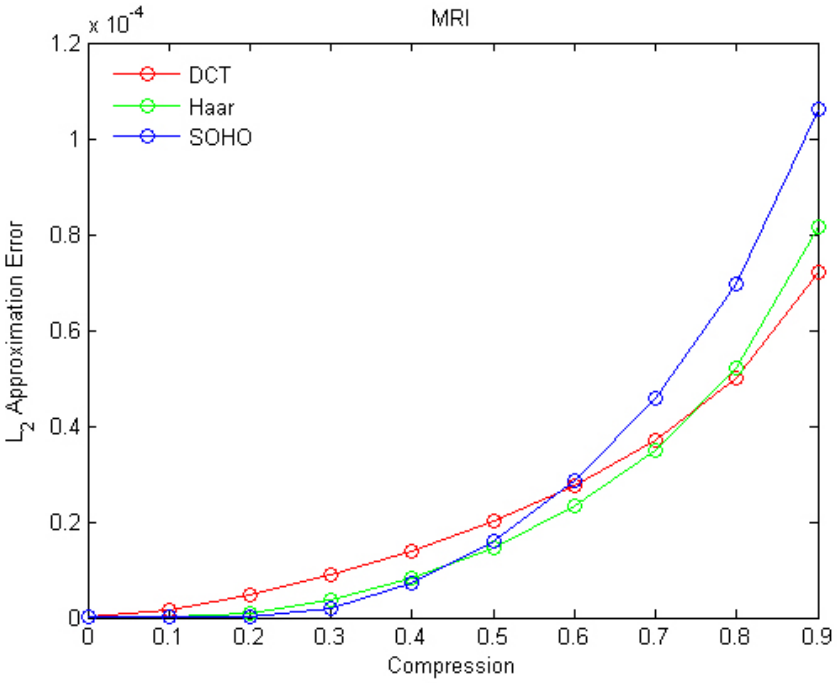

(b)

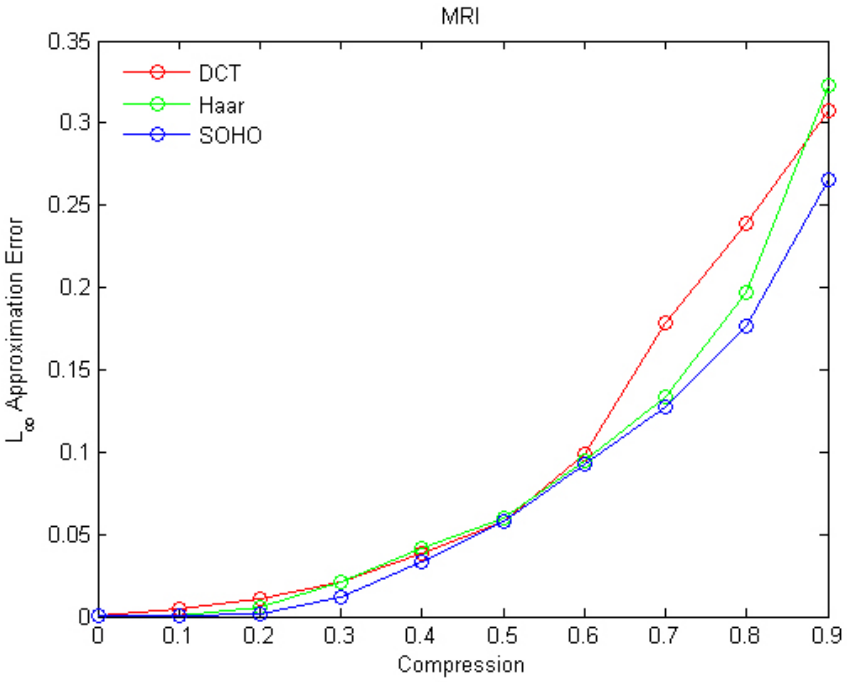
MRI
DCT
Haar
SOHO
L_∞ Approximation Error
Compression
0
0.05
0.1
0.15
0.2
0.25
0.3
0.35
0.1
0.2
0.3
0.4
0.5
0.6
0.7
0.8
0.9

(c)

Figure 5.12: Comparison of approximation performance on Perlin Noise A.

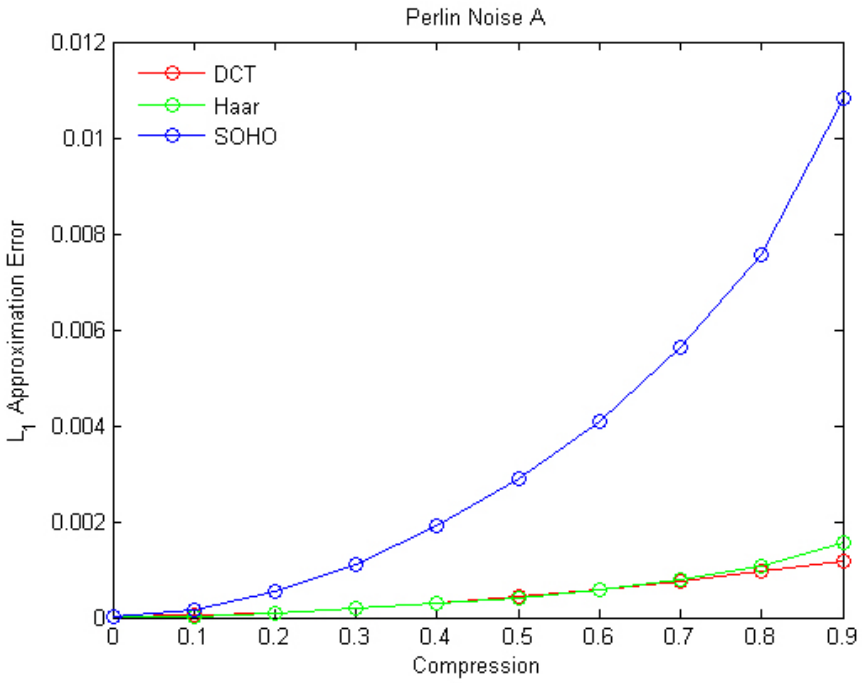

(a)

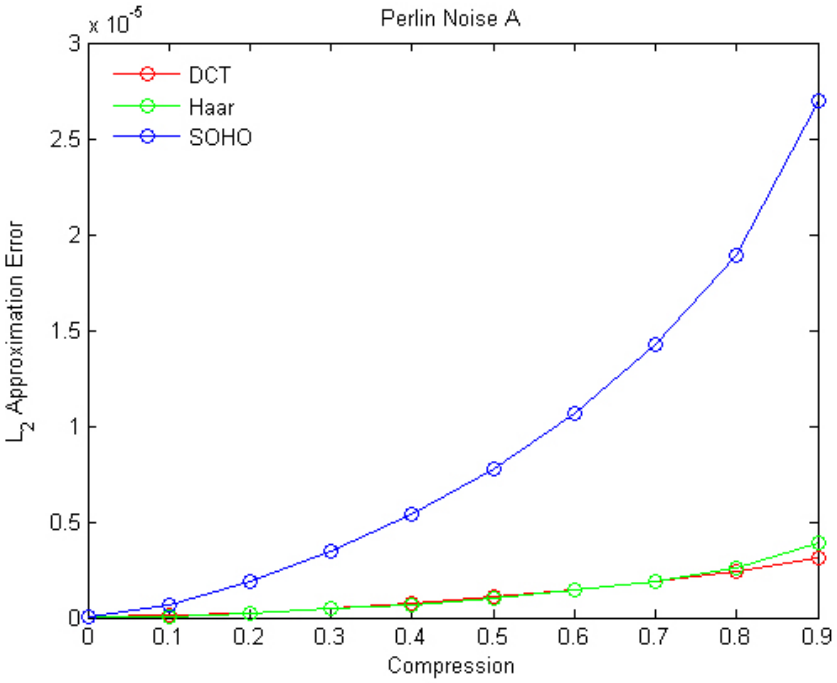

(b)

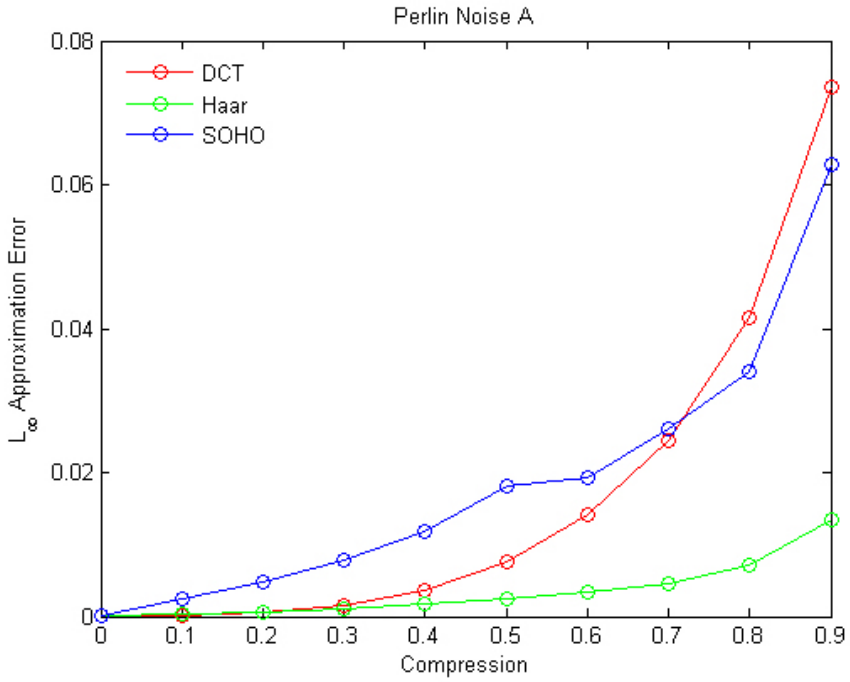
Perlin Noise A
DCT
Haar
SOHO
0.08
0.06
0.04
0.02
0
L_∞ Approximation Error
0
0.1
0.2
0.3
0.4
0.5
0.6
0.7
0.8
0.9
Compression

(c)

Figure 5.13: Comparison of approximation performance on Perlin Noise B.

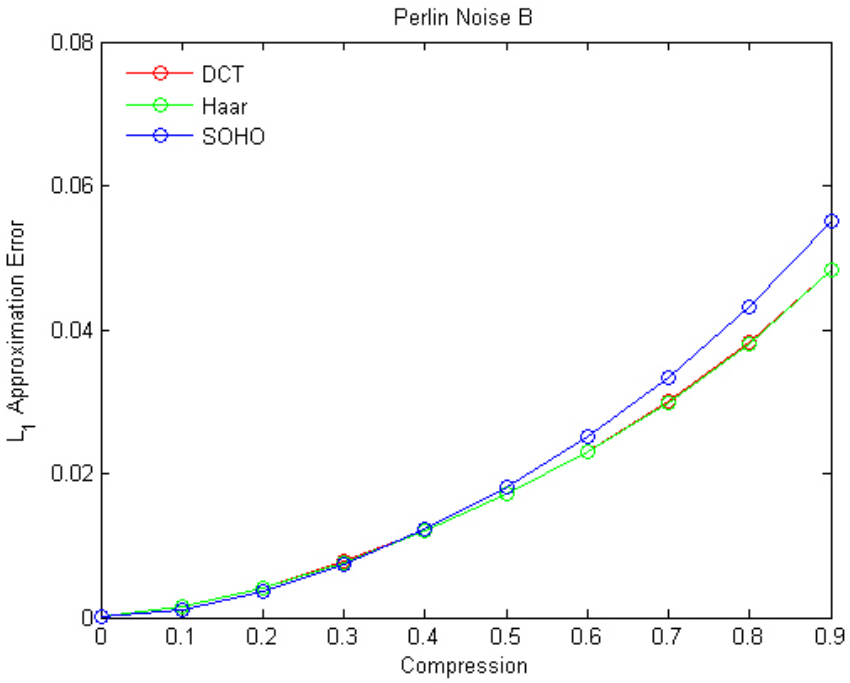

(a)

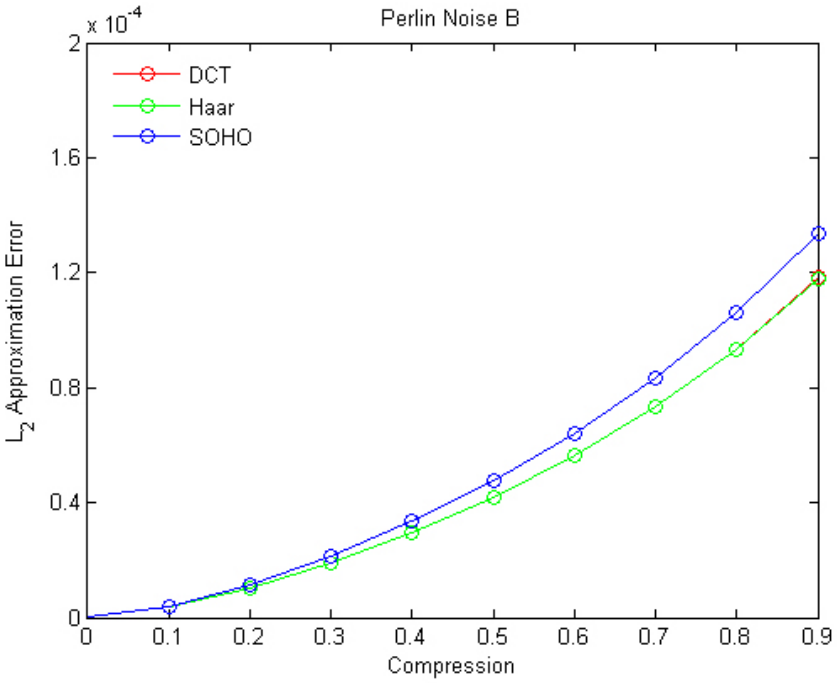

(b)

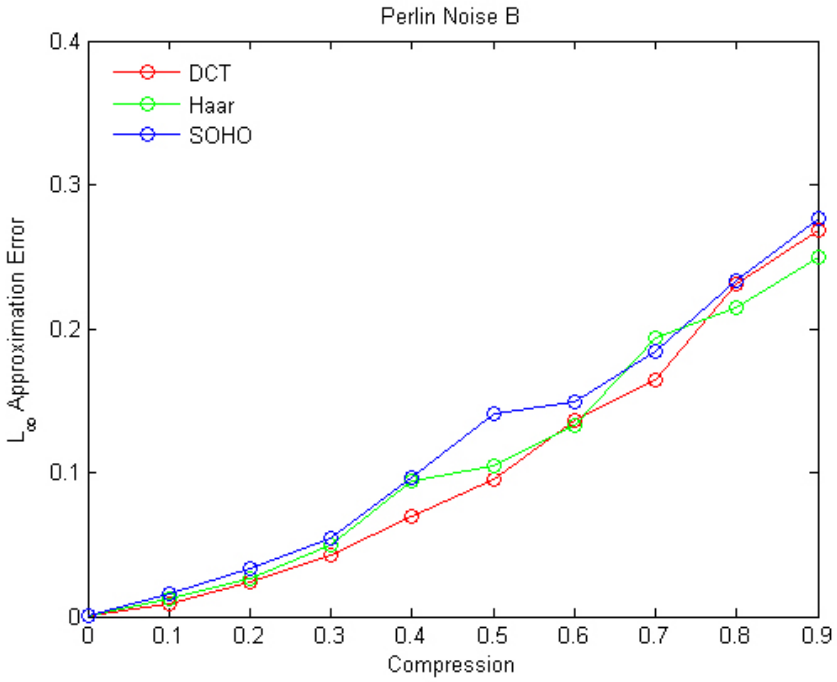
Perlin Noise B
DCT
Haar
SOHO
L∞ Approximation Error
Compression
0
0.1
0.2
0.3
0.4
0.5
0.6
0.7
0.8
0.9

(c)

Figure 5.14: Comparison of approximation performance on SLIMCAT.

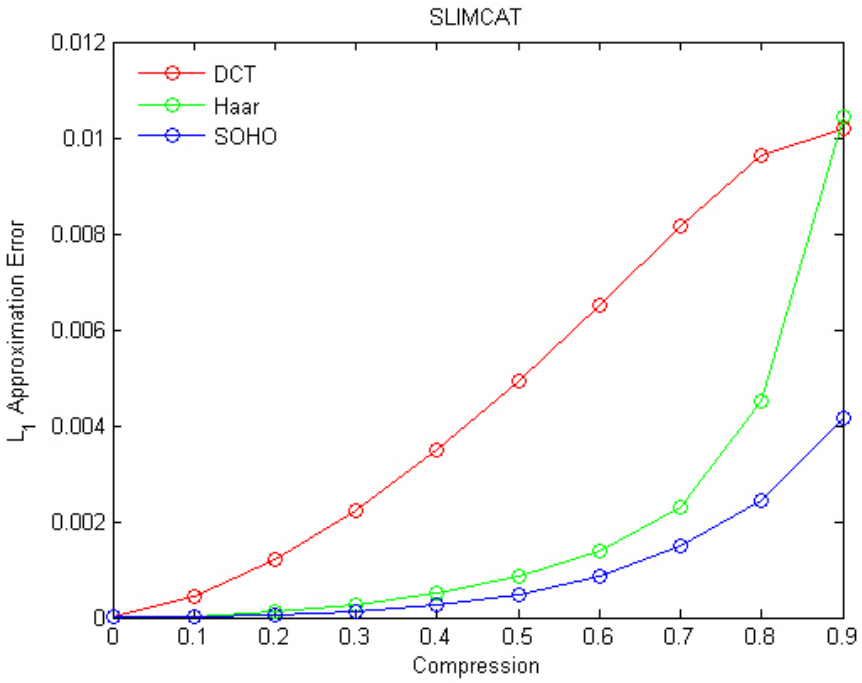

(a)

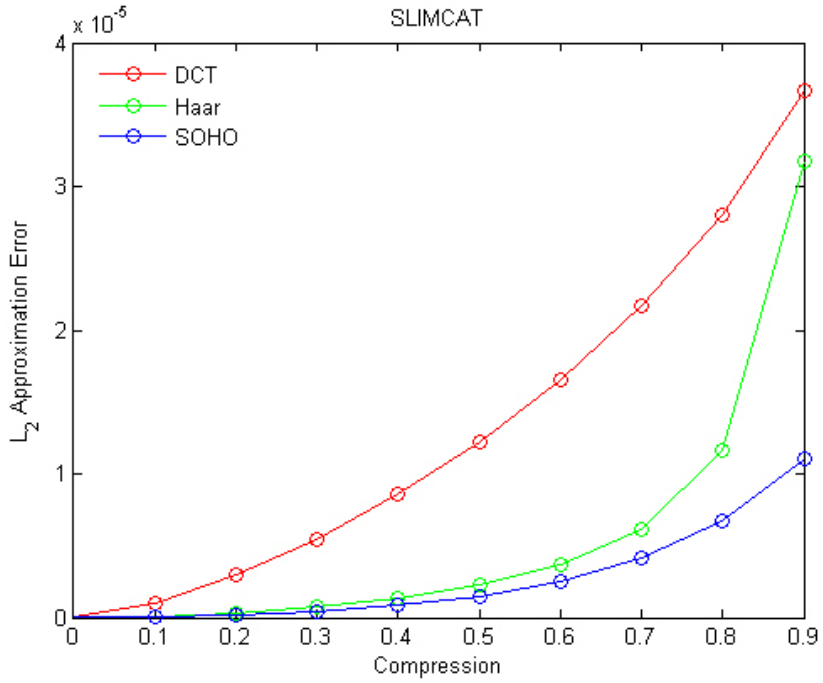

(b)

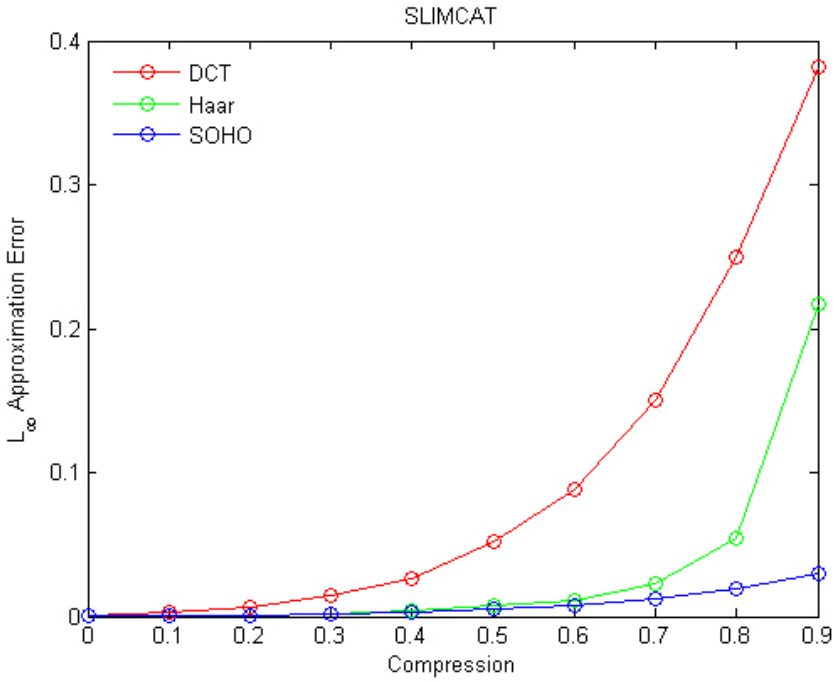
SLIMCAT
DCT
Haar
SOHO
L_∞ Approximation Error
Compression
0
0.1
0.2
0.3
0.4
0.5
0.6
0.7
0.8
0.9

(c)

Figure 5.15: Comparison of approximation performance on CBCT.

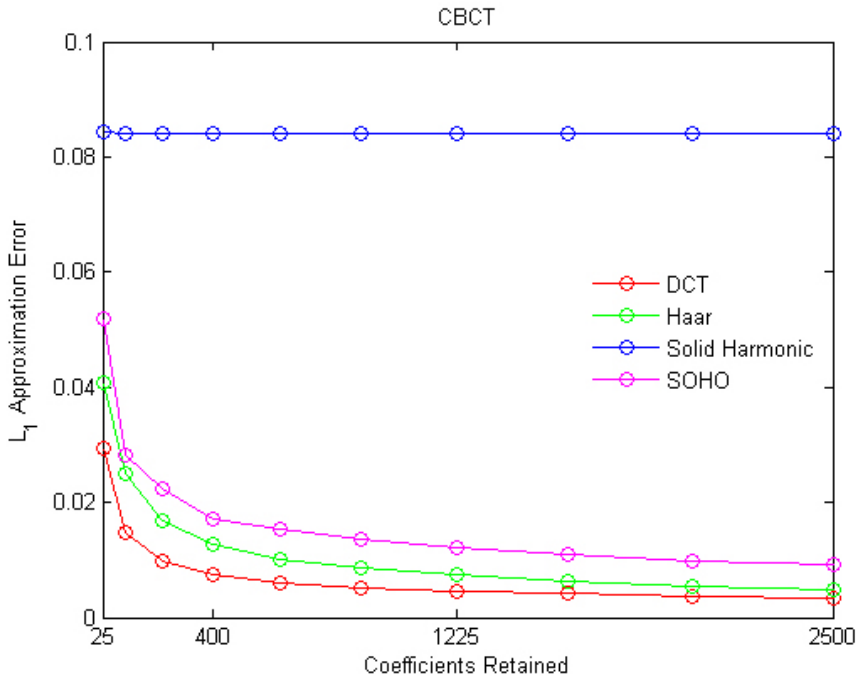

(a)

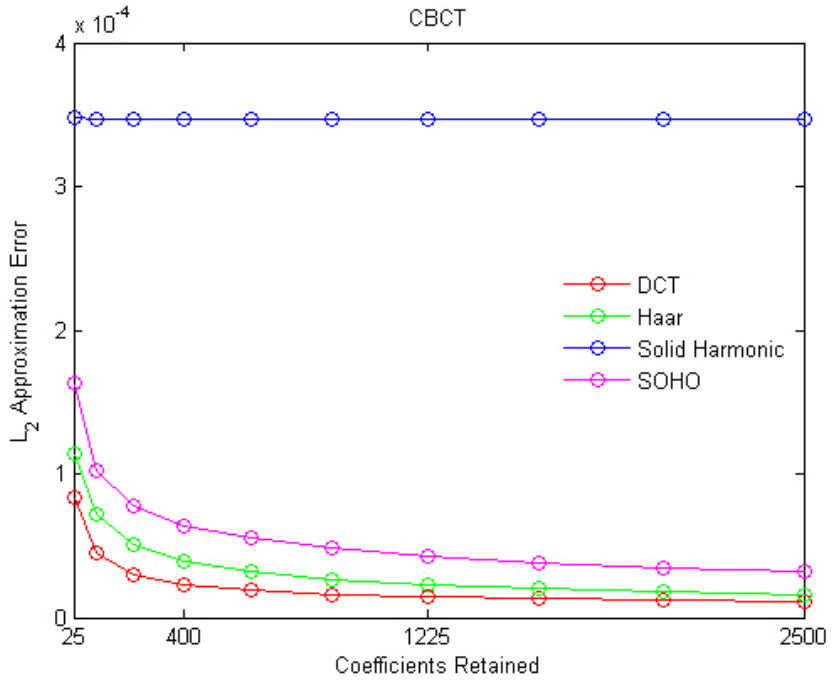

(b)

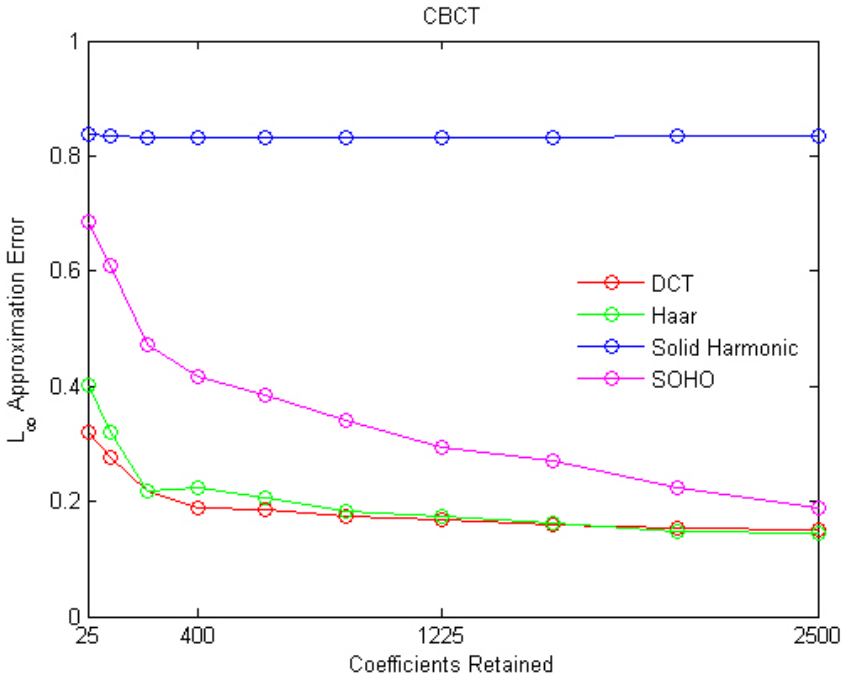
CBCT
1
0.8
0.6
0.4
0.2
0
L_∞ Approximation Error
25
400
1225
2500
Coefficients Retained
DCT
Haar
Solid Harmonic
SOHO

(c)

Figure 5.16: Comparison of approximation performance on SLIMCAT.

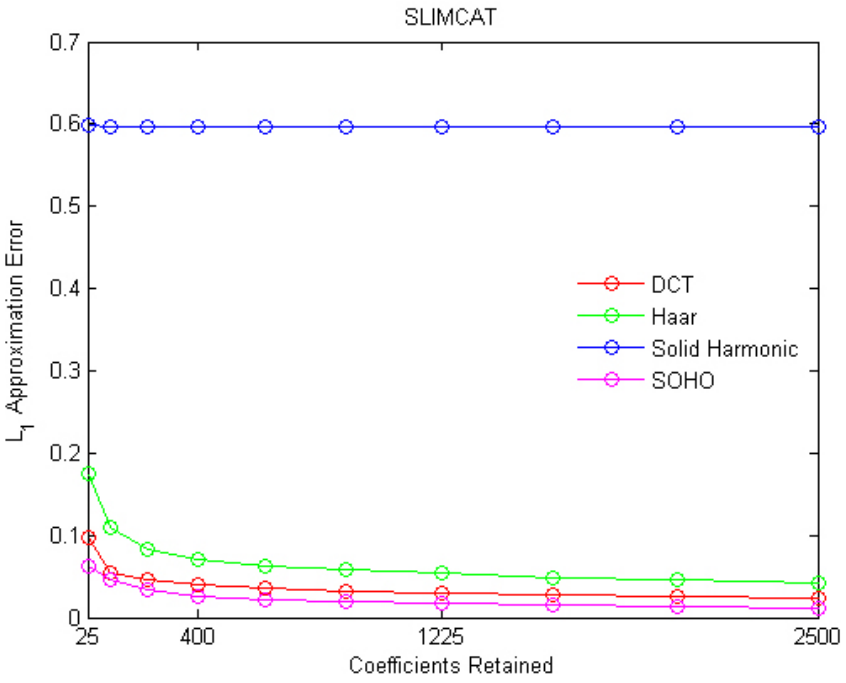

(a)

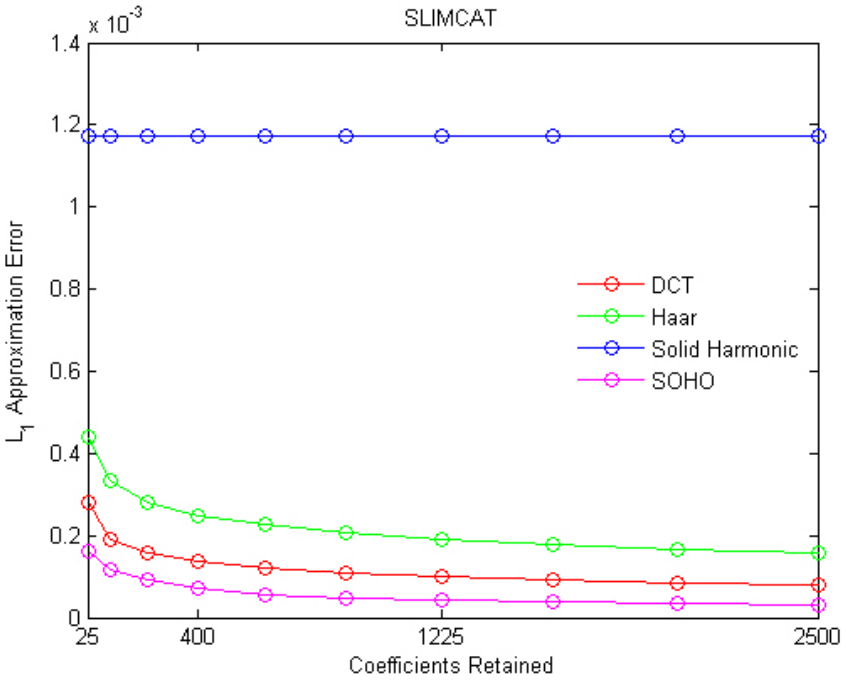

(b)

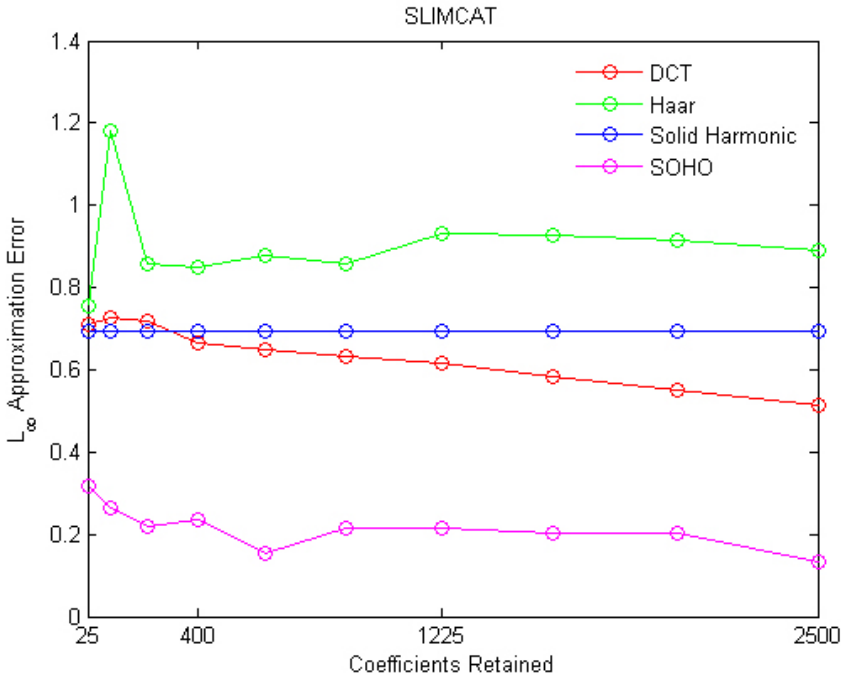
SLIMCAT
DCT
Haar
Solid Harmonic
SOHO
L∞ Approximation Error
Coefficients Retained
1.4
1.2
1
0.8
0.6
0.4
0.2
0
25
400
1225
2500

(c)

Figure 5.17: Approximation performance of Solid Harmonic on MRI.

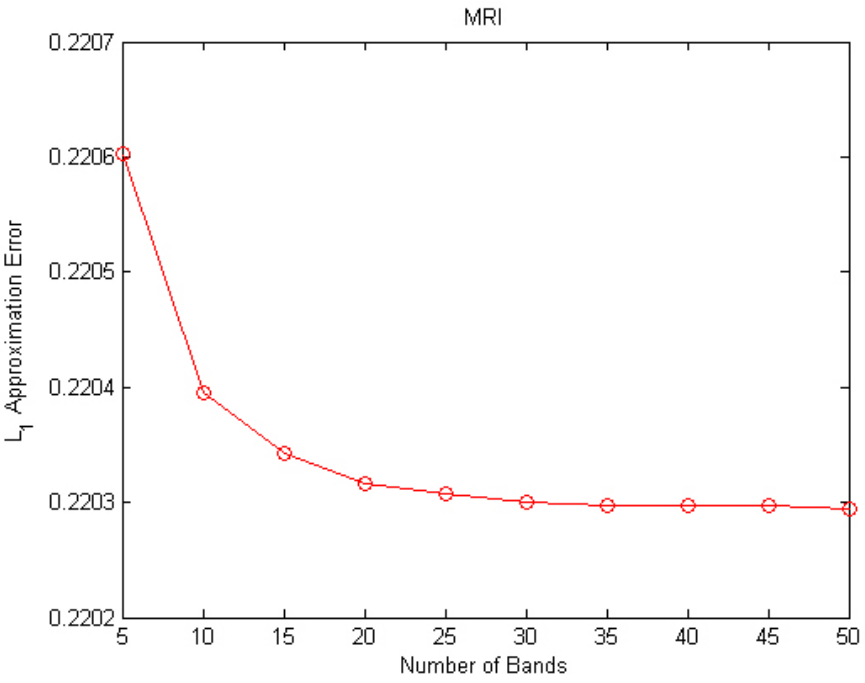

(a)

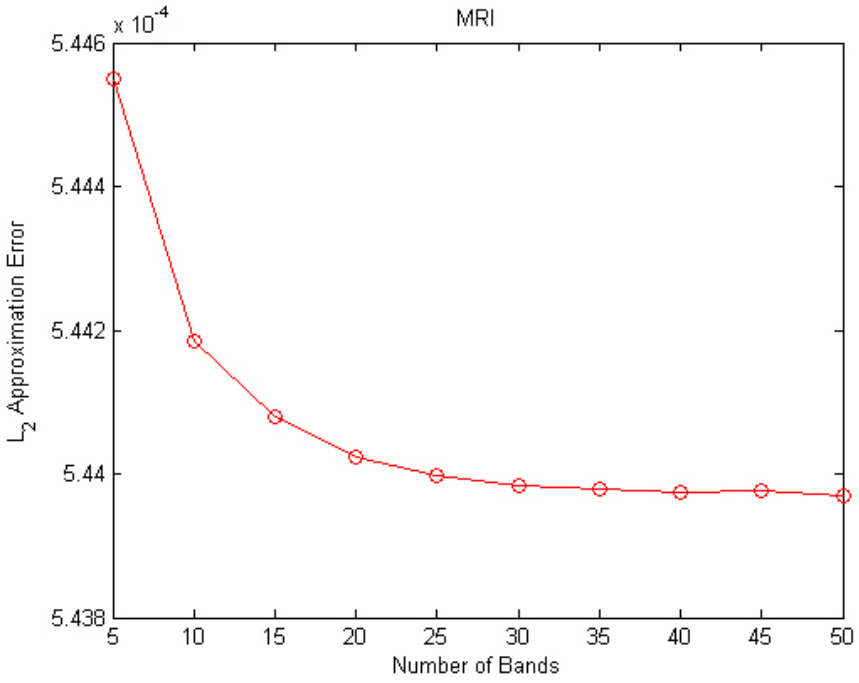

(b)

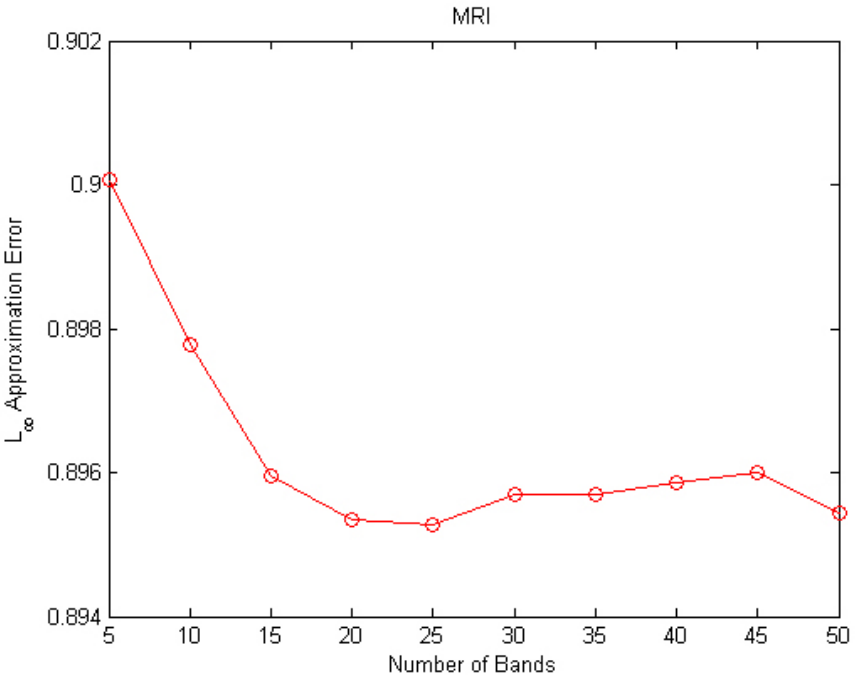
MRI
0.902
0.9
0.898
0.896
0.894
L_∞ Approximation Error
5
10
15
20
25
30
35
40
45
50
Number of Bands

(c)

Figure 5.18: Approximation performance of Solid Harmonic on CBCT.

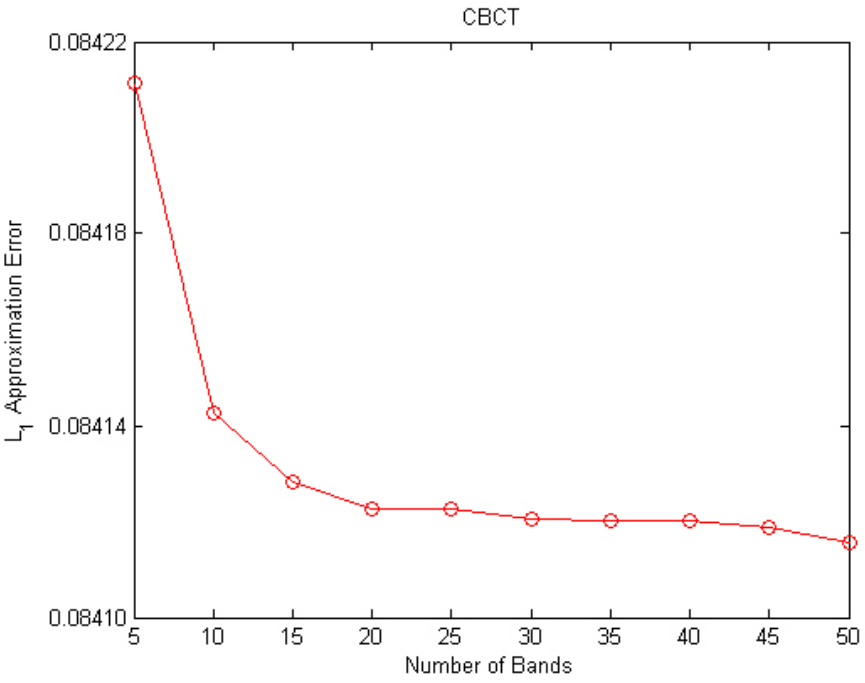

(a)

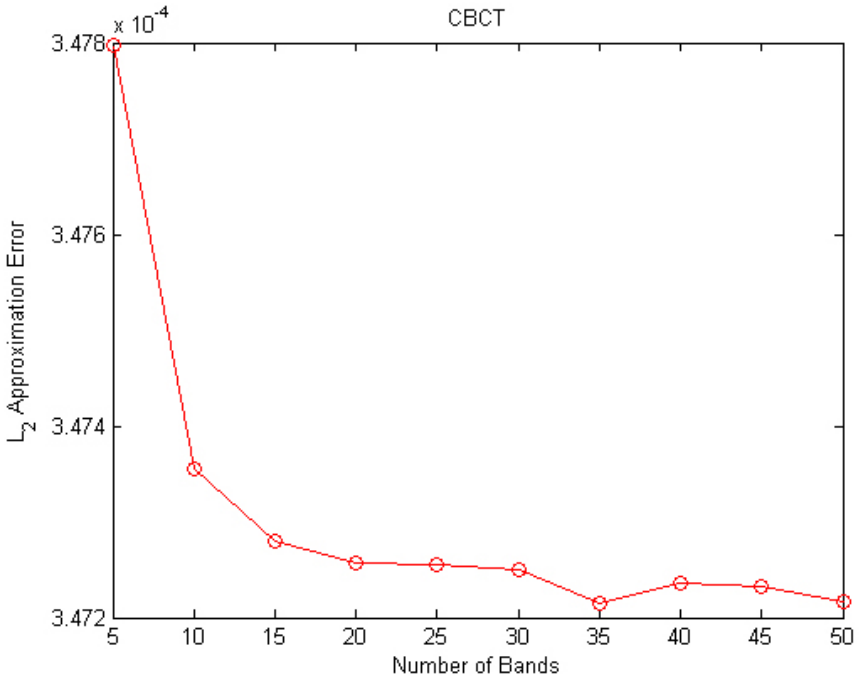

(b)

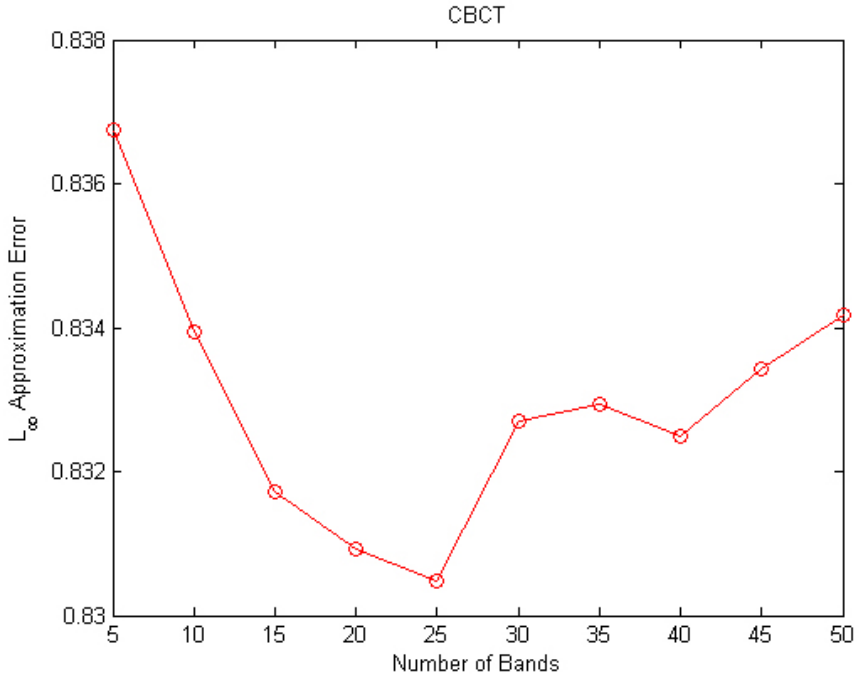

(c)

Figure 5.19: L^{∞} approximation error fluctuation.

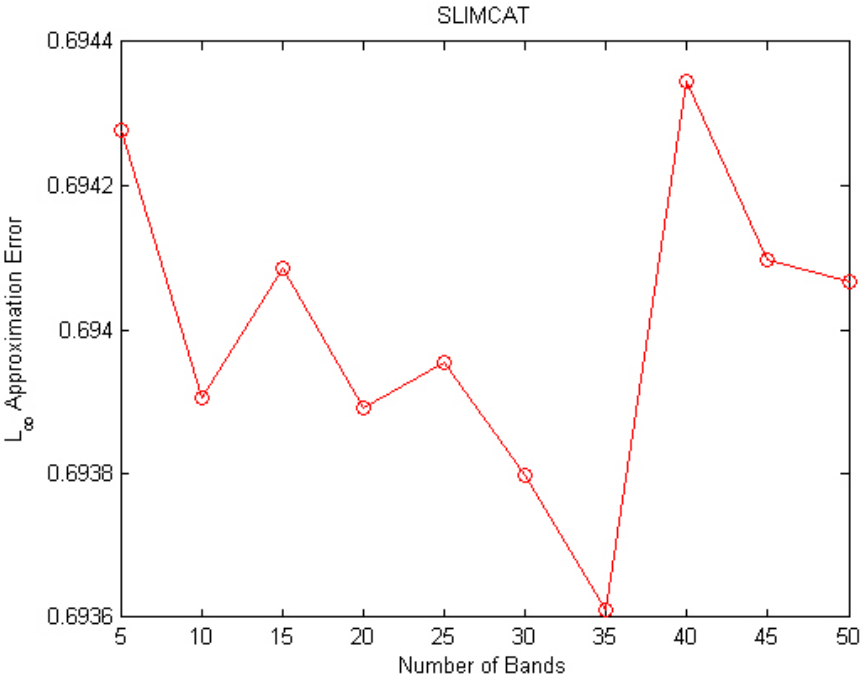

5.4 Discussion

In this section, we will interpret the results and draw some general conclusions about the nature of the 3D SOHO wavelet basis. We will use Ψ_+ and Ψ_- respectively, to denote the basis obtained by addition and subtraction in Equation 4.10. Likewise, the basis obtained from a tetrahedron, octahedron and icosahedron will be denoted as Ψ_T, Ψ_O and Ψ_I respectively.

5.4.1 Partition Performance

A SOHO partition has two construction parameters, namely the choice of platonic solid and the number of subdivision levels. Experiments were conducted to determine their effects on the resampling performance of SOHO. The results showed an exponential decrease in resampling error, as the number of levels increased (Figure 5.8). Similarly, the resampling error decreased as the number of trees in the partition increased (Figure 5.9). However, the type of platonic solid was insignificant for partitions with more than 3 levels. In summary, the resampling error was negatively correlated with the number of domains in a partition.

In addition, we examined the mean magnitude of the SOHO wavelet basis function coefficients. An exponential decay in mean magnitude was observed as the number of levels increased (Figure 5.5). In most cases, Ψ_- yielded slightly smaller means than Ψ_+. However, the difference was negligible for partitions with more than 3 levels (Figure 5.6). The mean magnitude was the largest for Ψ_T, followed by Ψ_O and then by Ψ_I (Figure 5.7). Nevertheless, the type of platonic solid was insignificant for partitions with more than 3 levels. In general, the mean magnitude was negatively correlated with the number of domains in a partition.

5.4.2 Approximation Performance

The approximation performance of DCT, Haar, SOHO and Solid Harmonic are shown in Figure 5.10 to Figure 5.16. In general, the ℓ_1, ℓ_2 and ℓ_∞ approximation errors increased exponentially as the space savings increased for all four bases. Exceptions occurred for some approximations in Solid Harmonic, where the ℓ_∞ error increased (Figure 5.19c) or fluctuated (Figure 5.19).

Comparisons between DCT, Haar and SOHO did not reveal a superior basis (Figure 5.10 to Figure 5.14). For instance, SOHO outperformed DCT and Haar for SLIMCAT (Figure 5.14), but the results were opposite for Perlin Noise (Figure 5.12 and Figure 5.13).

The k-largest approximation strategy is optimal in the ℓ_2 norm for orthonormal bases. However, it has been argued that the ℓ_1 norm is a better estimate for the perceived image quality [22]. Consequently, the subjective performance of SOHO depends on whether or not there is a positive correlation between the ℓ_1 and ℓ_2 approximation errors. The experiments showed that the ℓ_1 and ℓ_2 errors behave very similarly in general. Therefore we argue that the k-largest strategy is suitable for minimizing the ℓ_1 approximation error.

The approximation performance of Solid Harmonic was inferior to that of DCT, Haar and SOHO in every experiment (Figure 5.15 and Figure 5.16). Not only did Solid Harmonic consistently produced the highest approximation error, but the error did not decrease significantly as the number of coefficients increased. Differences were only be noticeable at finer scales (Figure 5.17 and Figure 5.18). Therefore, SOHO is better than Solid Harmonic at representing all-frequency signals in $L_2(\mathbb{B}^3)$.

Chapter 6

Future Work

A quantitative analysis of SOHO has been presented in Chapter 5. Nevertheless, qualitative evaluations are needed in order to determine the efficacy of SOHO in real-world applications. For instance, there are many unanswered questions related to the use of SOHO in medical imaging. Although we have evaluated SOHO on two medical data sets, a much larger sample size is required to draw any meaningful conclusions. Qualitative experiments involving real patients and medical doctors are also necessary. Differences in signal resolution, scanning apparatus and object geometry could play significant roles in the performance SOHO. Additional studies are needed to identify the conditions under which SOHO can outperform DCT, and other popular image compression techniques.

Some applications require the alignment of data sets. A well known example is the processing and analysis of spherical data sets in medical imaging. A method for performing rotation already exists for the two-dimensional SOHO wavelet basis. Naturally, we would like to discover a similar method for 3D SOHO.

Solid Harmonic is a basis for the frequency domain, where powerful mathematical tools are available for signal analysis and processing. Many of these techniques cannot be applied in the spatial domain. Therefore, discovering new ways to perform signal analysis in the SOHO wavelet basis would be very beneficial. Noise reduction is an obvious avenue, since multiresolution analysis is akin to Fourier analysis in the spatial domain. Perhaps valuable information can be distilled from the basis function coefficients, to assist in texture classification and image segmentation.

A *pseudo 3D SOHO partition* consists of a set of shells, where each shell is represented by a 2D SOHO partition. Consequently, the analysis and reconstruction of a pseudo partition can be performed in parallel on individual shells. It would be interesting to compare the approximation performance of pseudo 3D SOHO against that of 3D SOHO. Although pseudo 3D SOHO is not optimal in the ℓ_2 norm in general, it may be a reasonable trade-off between speed and accuracy.

Chapter 7

Conclusion

In this thesis, we developed the three-dimensional SOHO wavelet basis for representing all-frequency signals in $L_2(\mathbb{B}^3)$. To our knowledge, 3D SOHO is the first Haar wavelet basis on the solid sphere that is both orthogonal and symmetric. Such properties allow for fast wavelet transforms, perfect reconstruction and an optimal approximation strategy in the ℓ_2 norm.

Experimental results demonstrate the representation performance of 3D SOHO on various signals, including a CBCT projection set, a brain MRI data set and an atmospheric model. Resampling error is dominated by the number of subdivision levels in a partition. Other construction parameters, such as the choice of platonic solid, are insignificant for partitions with more than three levels.

Results also indicate similar approximation performances between DCT, Haar and SOHO, with neither one performing consistently better than the others. However, results confirm that SOHO is superior to Solid Harmonic in representing and approximating all-frequency signals on the three-dimensional ball.

Although the k-largest approximation strategy is not optimal in the ℓ_1 norm, the experiments reveal a positive correlation between the ℓ_1 and ℓ_2 errors. Therefore, k-largest is a reasonable approximation strategy in the ℓ_1 norm for the 3D SOHO wavelet basis.

The theoretical properties of 3D SOHO has been presented, and its performance has been affirmed by experimentation. We hope that our work will be utilized by others in the advancement of science, mathematics and engineering.

Bibliography

[1] Abel Amirbekyan and Volker Michel. Splines on the three-dimensional ball and their application to seismic body wave tomography. *Inverse Problems*, 24(1):1–25, 2008.

[2] Abel Amirbekyan, Volker Michel, and Frederik J. Simons. Parametrizing surface wave tomographic models with harmonic spherical splines. *Geophysical Journal International*, 174(2):617–628, 2008.

[3] Jean P. Antoine, Romain Murenzi, Pierre Vanderghynst, and Syed T. Ali. *Two-Dimensional Wavelets And Their Relatives*. Cambridge University Press, New York, NY, USA, 2004.

[4] Michael Antolik, Yu J. Gu, Göran Ekström, and Adam M. Dziewonski. J362d28: A new joint model of compressional and shear velocity in the earthś mantle. *Geophysical Journal International*, 153(2):443–466, 2003.

[5] Marc Antonini, Michel Barlaud, Pierre Mathieu, and Ingrid Daubechies. Image coding using wavelet transform. *IEEE Transactions On Image Processing*, 1(2):205–220, 1992.

[6] Alain Arneodo, Yves d'Aubenton Carafa, Emmanuel Bacry, P. V. Graves, Claude Thermes, and Jean-François Muzy. Wavelet based fractal analysis of dna se-

quences. *MSTD '95: Proceedings Of The Workshop On Measures Of Spatio-Temporal Dynamics*, pages 291–320, 1996.

[7] Albert Bijaoui, Eric Slezak, Frédéric Rué, and Elena Lega. Wavelets and the study of the distant universe. *Proceedings Of The IEEE*, 84(4):670–679, 1996.

[8] Emmanuel J. Candès. Harmonic analysis of neural networks. *Applied And Computational Harmonic Analysis*, 6(2):197–218, 1999.

[9] Philippe Carré and Eric Andres. Ridgelet transform based on reveillès discrete lines. *Proceedings Of The 10th International Conference On Discrete Geometry For Computer Imagery*, 2301:417–427, 2002.

[10] Mike Carson. Wavelets and molecular structure. *Journal Of Computer-Aided Molecular Design*, 10(4):273–283, 1996.

[11] Ling-Yun Chiao and Ban-Yuan Kuo. Multiscale seismic tomography. *Geophysical Journal International*, 145(2):517–527, 2001.

[12] Martyn P. Chipperfield, Michelle L. Santee, Lucien Froidevaux, Gloria L Manney, William G. Read, Joe W. Waters, Aidan E. Roche, and James M. Russell. Analysis of uars data in the southern polar vortex in september 1992 using a chemical transport model. *Journal Of Geophysical Research*, 101(D13):18861–18881, 1996.

[13] Youngbin Cho, Douglas J. Moseley, Jeffrey H. Siewerdsen, and David A. Jaffray. Accurate technique for complete geometric calibration of cone-beam computed tomography systems. *Medical Physics*, 32(4):968–983, 2005.

[14] Ole Christensen. *Frames and Bases: An Introductory Course*. Applied And Numerical Harmonic Analysis. Birkhäuser Boston, Cambridge, MA, USA, 2008.

[15] Per H. Christensen, Eric J. Stollnitz, David H. Salesin, and Tony D. DeRose. Global illumination of glossy environments using wavelets and importance. *ACM Transactions On Graphics*, 15(1):37–71, 1996.

[16] Charles K. Chui. *An Introduction To Wavelets*, volume 1 of *Wavelet Analysis And Its Applications*. Academic Press, San Diego, CA, USA, third edition, 1992.

[17] Chris A. Cocosco, Vasken Kollokian, Remi K. S. Kwan, and Alan C. Evans. Brainweb: Online interface to a 3d mri simulated brain database. *NeuroImage*, 5(4):425, 1997.

[18] D. Louis Collins, Alex P. Zijdenbos, Vasken Kollokian, John G. Sled, Noor J. Kabani, Colin J. Holmes, and Alan C. Evans. Design and construction of a realistic digital brain phantom. *IEEE Transactions On Medical Imaging*, 17(3):463–468, 1998.

[19] Ingrid Daubechies. Where do wavelets come from? a personal point of view. *Proceedings Of The IEEE*, 84(4):510–513, 1996.

[20] Ingrid Daubechies and Wim Sweldens. Factoring wavelet transforms into lifting steps. *Journal Of Fourier Analysis And Applications*, 4(3):247–269, 1998.

[21] Lucia Dettori and Ahmed I. Zayed. Texture identification of tissues using directional wavelet, ridgelet, and curvelet transforms. *Frames And Operator Theory In Analysis And Signal Processing*, 451:89–118, 2008.

[22] Ronald A. DeVore, Björn Jawerth, and Bradley J. Lucier. Image compression through wavelet transform coding. *IEEE Transactions On Information Theory*, 38(2):719–746, 1992.

[23] David L. Donoho. Orthonormal ridgelets and linear singularities. *SIAM Journal On Mathematical Analysis*, 31(5):1062–1099, 2000.

[24] David L. Donoho and Ana G. Flesia. Digital ridgelet transform based on true ridge functions. In Grant V. Welland, editor, *Beyond Wavelets*, pages 1–30. Academic Press, San Diego, CA, USA, 2003.

[25] Eric Escalera and Harvey MacGillivray. Topology in galaxy distributions: Method for a multi-scale analysis. a use of the wavelet transform. *Astronomy And Astrophysics*, 298:1–21, 1995.

[26] Mohamed J. Fadili and Jean-Luc Starck. Curvelets and ridgelets. In Robert A. Meyers, editor, *Encyclopedia Of Complexity And Systems Science*, pages 1–30. Springer, 2007.

[27] Li-Zhi Fang and Long long Feng. Measuring the galaxy power spectrum and scale-scale correlations with multiresolution-decomposed covariance. i. method. *The Astrophysical Journal*, 539:5–19, 2000.

[28] Timothy G. Feeman. *Portraits Of The Earth: A Mathematician Looks At Maps*. American Mathematical Society, Providence, RI, USA, 2002.

[29] Martin J. Fengler, Dominik Michel, and Volker Michel. Harmonic spline-wavelets on the 3-dimensional ball and their application to the reconstruction of the earthś density distribution from gravitational data at arbitrarily shaped satellite orbits. *Journal Of Applied Mathematics And Mechanics*, 86(11):856–873, 2006.

[30] Maria Girardi and Wim Sweldens. A new class of unbalanced haar wavelets that form an unconditional basis for lp on general measure spaces. *Journal Of Fourier Analysis And Applications*, 3(4):457–474, 1997.

[31] Jaideva C. Goswami and Andrew K. Chan. *Fundamentals Of Wavelets: Theory, Algorithms, And Applications*. Wiley-Interscience, New York, NY, USA, 1999.

[32] Robin Green. Spherical harmonic lighting: The gritty details. In *Game Developers Conference*, 2003.

[33] Addison Greenwood. *Science At The Frontier*. National Academy Press, Washington, DC, USA, 1992.

[34] Yu J. Gu, Adam M. Dziewonski, Weijia Su, and Göran Ekström. Models of the mantle shear velocity and discontinuities in the pattern of lateral heterogeneities. *Journal Of Geophysical Research*, 106(B6):11169–11199, 2001.

[35] Dominique Guegan and Kebira Hoummiya. De-noising with wavelets method in chaotic time series: Application in climatology, energy and finance. *Proceedings Of The SPIE*, 5848:174–185, 2005.

[36] Trevor Hastie, Robert Tibshirani, and Jerome H. Friedman. *The Elements Of Statistical Learning: Data Mining, Inference, And Prediction*. Springer, 2001.

[37] Michiel Hazewinkel. *Encyclopaedia Of Mathematics*, chapter Ridge Function (41A30,92C55). Springer, third edition, 2002.

[38] Christopher Heil and David F. Walnut. *Fundamental Papers In Wavelet Theory*. Princeton University Press, Princeton, NJ, USA, 2006.

[39] Ataollah A. Hemmat, Mohammad A. Dehghan, and Maria A. Skopina. Ridge wavelets on the ball. *Journal Of Approximation Theory*, 136(2):129–139, 2005.

[40] Hideki Hirakawa, Shigeru Muta, and Satoru Kuhara. The hydrophobic cores of proteins predicted by wavelet analysis. *Bioinformatics*, 15(2):141–148, 1999.

[41] Barbara B. Hubbard. *The World According To Wavelets: The Story Of A Mathematical Technique In The Making*. AK Peters, Ltd., Natick, MA, USA, 1998.

[42] Irina Kezele, Maxime Descoteaux, Cyril Poupon, Pierrick Abrial, Fabrice Poupon, and Jean-François Mangin. Multiresolution decomposition of hardi and odf profiles using spherical wavelets. In *Workshop On Computational Diffusion MRI*, 2008.

[43] Tae-Young Kim and Yeong Gil Shin. An efficient wavlet-based compression method for volume rendering. *Proceedings Of The 7th Pacific Conference On Computer Graphics And Applications*, pages 147–156, 1999.

[44] Robert R. Klevecz. Dynamic architecture of the yeast cell cycle uncovered by wavelet decomposition of expression microarray data. *Functional And Integrative Genomics*, 1(3):186–192, 2000.

[45] Remi K. S. Kwan, Alan C. Evans, and G. Bruce Pike. An extensible mri simulator for post-processing evaluation. *Lecture Notes In Computer Science*, 1131:135–140, 1996.

[46] Remi K. S. Kwan, Alan C. Evans, and G. Bruce Pike. Mri simulation-based evaluation of image-processing and classification methods. *IEEE Transactions On Medical Imaging*, 18(11):1085–1097, 1999.

[47] Christian Lessig. Orthogonal and symmetric haar wavelets on the sphere. Master's thesis, Department Of Computer Science, University Of Toronto, 2007.

[48] Christian Lessig and Eugene Fiume. Soho: Orthogonal and symmetric haar wavelets on the sphere. *ACM Transactions On Graphics*, 27(1), 2008.

[49] Joram Lindenstrauss and Lior Tzafriri. *Classical Banach Spaces*. Lecture Notes In Mathematics. Springer Berlin, 1973.

[50] Zicheng Liu, Steven J. Gortler, and Michael F. Cohen. Hierarchical spacetime control. *In Proceedings Of The 21st Annual Conference On Computer Graphics And Interactive Techniques*, pages 35–42, 1994.

[51] Guy Masters, Stuart Johnson, Gabi Laske, and Harold Bolton. A shear-velocity model of the mantle. *Philosophical Transactions: Mathematical, Physical And Engineering Sciences*, 354(1711):1385–1411, 1996.

[52] The MathWorks. Matlab 7 programming fundamentals.

[53] Jason D. McEwen, Patricio Vielva, Michael P. Hobson, Enrique Martinez-Gonzalez, and Anthony N. Lasenby. Detection of the isw effect and corresponding dark energy constraints made with directional spherical wavelets. *Monthly Notices Of The Royal Astronomical Society*, 376(3):1211–1226, 2007.

[54] Jason D. McEwen, Patricio Vielva, Yves Wiaux, Rita B. Barreiro, Laura Cayón, Michael P. Hobson, Anthony N. Lasenby, Enrique Martinez-Gonzalez, and Jorge L. Sanz. Cosmological applications of a wavelet analysis on the sphere. *Journal Of Fourier Analysis And Applications*, 13(4):495–510, 2007.

[55] Yves Meyer. *Wavelets: Algorithms & Applications*. Society For Industrial And Applied Mathematics, Philadelphia, PA, USA, 1993.

[56] Steven D. Meyers, Brian G. Kelly, and James J. O'Brien. An introduction to wavelet analysis in oceanography and meteorology: With application to the dispersion of yanai waves. *Monthly Weather Review*, 121(10):2858–2866, 1993.

[57] Volker Michel. Scale continuous, scale discretized, and scale discrete harmonic wavelets for the outer and the inner space of a sphere and their application to an inverse problem in geomathematics. *Applied And Computational Harmonic Analysis*, 12(1):77–99, 2002.

[58] Volker Michel. Regularized wavelet-based multiresolution recovery of the harmonic mass density distribution from data of the earth's gravitational field at satellite height. *Inverse Problems*, 21(3):997–1025, 2005.

[59] Volker Michel. Wavelets on the 3-dimensional ball. *Proceedings In Applied Mathematics And Mechanics*, 5(1):775–776, 2005.

[60] Volker Michel and Kerstin Wolf. Numerical aspects of a spline-based multiresolution recovery of the harmonic mass density out of gravity functionals. *Geophysical Journal International*, 173(1):1–16, 2008.

[61] Martin J. Mohlenkamp. A fast transform for spherical harmonics. *Journal Of Fourier Analysis And Applications*, 5(2-3):159–184, 1999.

[62] Yassir Moudden, Jean-François Cardoso, Jean-Luc Starck, and Jacques Delabrouille. Blind component separation in wavelet space. application to cmb analysis. *EURASIP Journal On Applied Signal Processing*, pages 2437–2454, 2005.

[63] Kevin B. Murray, Denise Gorse, and Janet M. Thornton. Wavelet transforms for the characterization and detection of repeating motifs. *Journal Of Molecular Biology*, 316(2):341–363, 2002.

[64] Delphine Nain, Steven Haker, Aaron F. Bobick, and Allen Tannenbaum. Multiscale 3d shape representation and segmentation using spherical wavelets. *IEEE Transactions On Medical Imaging*, 26(4):598–618, 2007.

[65] Delphine Nain, Martin A. Styner, Marc Niethammer, James J. Levitt, Martha E. Shenton, Guido Gerig, Aaron F. Bobick, and Allen Tannenbaum. Statistical shape analysis of brain structures using spherical wavelets. *Proceedings Of The 4th IEEE International Symposium On Biomedical Imaging: From Nano To Macro 2007*, pages 209–212, 2007.

[66] Ren Ng, Ravi Ramamoorthi, and Pat Hanrahan. All-frequency shadows using non-linear wavelet lighting approximation. *ACM Transactions On Graphics*, 22(3):376–381, 2003.

[67] Gregory M. Nielson, Il-Hong Jung, and Junwon Sung. Haar wavelets over triangular domains with applications to multiresolution models for flow over a sphere. *VIS '97: Proceedings Of The 8th Conference On Visualization '97*, pages 143–149, 1997.

[68] Ken Perlin. An image synthesizer. *SIGGRAPH '85: Proceedings Of The 12th Annual Conference On Computer Graphics And Interactive Techniques*, 19(3):287–296, 1985.

[69] Ken Perlin and Eric M. Hoffert. Hypertexture. *SIGGRAPH '89: Proceedings Of The 16th Annual Conference On Computer Graphics And Interactive Techniques*, 23(3):253–262, 1989.

[70] Pencho P. Petrushev. Approximation by ridge functions and neural networks. *SIAM Journal On Mathematical Analysis*, 30(1):155–189, 1999.

[71] James Cooper Robinson. *Infinite-Dimensional Dynamical Systems*. Cambridge University Press, 2001.

[72] Peter Schröder. Wavelets in computer graphics. *Proceedings Of The IEEE*, 84(4):615–625, 1996.

[73] Peter Schröder and Wim Sweldens. Spherical wavelets: Efficiently representing functions on the sphere. *SIGGRAPH '95: Proceedings Of The 22nd Annual Conference On Computer Graphics And Interactive Techniques*, pages 161–172, 1995.

[74] Julian S. Schwinger, Lester L. Deraad Jr., Kimball A. Milton, Wu yang Tsai, and Joyce Norton. *Classical Electrodynamics*. Westview Press, Boulder, CO, USA, 1998.

[75] Lindsay Semler and Lucia Dettori. *A Comparison Of Wavelet-Based And Ridgelet-Based Texture Classification Of Tissues In Computed Tomography*, volume 4 of *Communications In Computer And Information Science*. Springer Berlin, 2008.

[76] Lindsay Semler, Lucia Dettori, and Brandon Kerr. Ridgelet-based texture classification of tissues in computed tomography. *Proceedings Of The Eighth IASTED International Conference On Signal And Image Processing*, 2006.

[77] Kiran K. Simhadri, S. S. Iyengar, Ronald J. Holyer, Matthew Lybanon, and John M. Zachary Jr. Wavelet-based feature extraction from oceanographic images. *IEEE Transactions On Geoscience And Remote Sensing*, 36(3):767–778, 1998.

[78] Jean-Luc Starck, Vicent J. Martinez, and Enn Saar. *Multiscale Geometric Analysis Of The 2DF Data*. Statistical Problems In Particle Physics, Astrophysics

and Cosmology: Proceedings Of PHYSTAT05. Imperial College Press, London, UK, 2006.

[79] Jean-Luc Starck, Yassir Moudden, Pierrick Abrial, and Mai Nguyen. Wavelets, ridgelets and curvelets on the sphere. *Astronomy And Astrophysics*, 446:1191–1204, 2005.

[80] Jean-Luc Starck and Fionn Murtagh. *Astronomical Image And Data Analysis*. Springer Berlin, 2006.

[81] Eric J. Stollnitz, Tony D. Derose, and David H. Salesin. Wavelets for computer graphics: A primer, part 2. *IEEE Computer Graphics And Applications*, 15(4):75–85, 1995.

[82] Eric J. Stollnitz, Tony D. Derose, and David H. Salesin. *Wavelets For Computer Graphics: Theory and Applications*. Morgan Kaufmann, 1996.

[83] Wei-Jia Su and Adam M. Dziewonski. Simultaneous inversion for 3d variations in shear and bulk velocity in the mantle. *Physics Of The Earth And Planetary Interiors*, 100:135–156, 1997.

[84] Wim Sweldens. Lifting scheme: A new philosophy in biorthogonal wavelet constructions. *Proceedings Of The SPIE*, 2569:68–79, 1995.

[85] Wim Sweldens. The lifting scheme: A construction of second generation wavelets. *SIAM Journal On Mathematical Analysis*, 29(2):511–546, 1997.

[86] Wim Sweldens and Peter Schröder. Building your own wavelets at home. *Wavelets In Computer Graphics*, pages 15–87, 1996.

[87] Nobunao Takeuchi, Ken' Ichi Narita, and Yukihiro Goto. Wavelet analysis of meteorological variables under winter thunderclouds over the japan sea. *Journal Of Geophysical Research*, 99(D5):10751–10757, 1994.

[88] Anthony Teolis. *Computational Signal Processing With Wavelets*. Birkhäuser Boston, Cambridge, MA, USA, 1998.

[89] Robert J. A. Tough and Anthony J. Stone. Properties of the regular and irregular solid harmonics. *Journal Of Physics A: Mathematical And General*, 10(8):1261–1269, 1977.

[90] Carl C. Tscherning. Isotropic reproducing kernels for the inner of a sphere or spherical shell and their use as density covariance functions. *Mathematical Geology*, 28(2):161–168, 1996.

[91] Patricio Vielva. Probing the gaussianity and the statistical isotropy of the cmb with spherical wavelets. *Proceedings Of The SPIE*, 6701:1–17, 2007.

[92] Patricio Vielva, Enrique Martinez-Gonzalez, Julio E. Gallegos, Luigi Toffolatti, and Jorge L. Sanz. Point source detection using the spherical mexican hat wavelet on simulated all-sky planck maps. *Monthly Notices Of The Royal Astronomical Society*, 344(1):89–104, 2003.

[93] David F. Walnut. *An Introduction To Wavelet Analysis*. Birkhäuser Boston, Cambridge, MA, USA, 2004.

[94] Rui Wang, Ren Ng, David Luebke, and Greg Humphreys. Efficient wavelet rotation for environment map rendering. *Rendering Techniques 2006: 17th Eurographics Workshop On Rendering*, pages 173–182, 2006.

[95] Catherine Westbook and Carolyn Kaut. *MRI In Practice*. Blackwell Science, Oxford, England, UK, 1998.

[96] Boon-Lock Yeo and Bede Liu. Volume rendering of dct-based compressed 3d scalar data. *IEEE Transactions On Visualization And Computer Graphics*, 1(1):29–43, 1995.

[97] Boon Thye Thomas Yeo, Peng Yu, P. Ellen Grant, Bruce Fischl, and Polina Golland. Shape analysis with overcomplete spherical wavelets. *Proceedings Of The 11th International Conference On Medical Image Computing And Computer-Assisted Intervention*, 5241:468–476, 2008.

[98] Robert M. Young. *An Introduction To Nonharmonic Fourier Series*. Academic Press, San Diego, CA, USA, second edition, 2001.

[99] Peng Yu, P. Ellen Grant, Yuan Qi, Xiao Han, Florent Ségonne, Rudolph Pienaar, Evelina Busa, Jenni Pacheco, Nikos Makris, Randy L. Buckner, Polina Golland, and Bruce Fischl. Cortical surface shape analysis based on spherical wavelets. *IEEE Transactions On Medical Imaging*, 26(4):582–597, 2007.